Evolution of enhanced innate immune suppression by SARS-CoV-2 Omicron subvariants

Ann-Kathrin Reuschl[1], Lucy G. Thorne[1,2], Matthew V.X. Whelan[1], Roberta Ragazzini[1,3], Wilhelm Furnon[4], Vanessa M. Cowton[4], Giuditta de Lorenzo[4], Dejan Mesner[1], Jane L. E. Turner[1], Giulia Dowgier[5], Nathasha Bogoda[1], Paola Bonfanti[1,3], Massimo Palmarini[4], Arvind H. Patel[4], Clare Jolly[1*] and Greg. J. Towers[1*]

[1]Division of Infection and Immunity, University College London, WC1E 6BT London, United Kingdom. [2]Department of Infectious Diseases, St Mary's Medical School, Imperial College London, UK. [3]Epithelial Stem Cell Biology and Regenerative Medicine Laboratory, The Francis Crick Institute, London, NW1 1AT, United Kingdom. [4]MRC-University of Glasgow Centre for Virus Research, Glasgow, G61 1QH, United Kingdom. [5]COVID Surveillance Unit, The Francis Crick Institute, London, UK.

* These authors contributed equally.

Co-Corresponding authors:

Ann-Kathrin Reuschl a.reuschl@ucl.ac.uk

Clare Jolly c.jolly@ucl.ac.uk

Greg J. Towers g.towers@ucl.ac.uk

Keywords: SARS-CoV-2, VOC, Omicron, COVID-19, innate immunity, Orf6

SARS-CoV-2 adaptation to humans is evidenced by the emergence of variants of concern (VOCs) with distinct genotypes and phenotypes that facilitate immune escape and enhance transmission frequency. Most recently Omicron subvariants have emerged with heavily mutated spike proteins which facilitate re-infection of immune populations through extensive antibody escape driving replacement of previously-dominant VOCs Alpha and Delta. Interestingly, Omicron is the first VOC to produce distinct subvariants. Here, we demonstrate that later Omicron subvariants, particularly BA.4 and BA.5, have evolved an enhanced capacity to suppress human innate immunity when compared to earliest subvariants BA.1 and BA.2. We find that, like previously dominant VOCs, later Omicron subvariants tend to increase expression of viral innate immune antagonists Orf6 and nucleocapsid. We show Orf6 to be a key contributor to enhanced innate immune suppression during epithelial replication by BA.5 and Alpha, reducing innate immune signaling through IRF3 and STAT1. Convergent VOC evolution of enhanced innate immune antagonist expression suggests common pathways of adaptation to humans and links VOC, and in particular Omicron subvariant, dominance to improved innate immune evasion.

Alpha, Delta and Omicron have been sequentially globally dominant, with each VOC evolving independently from early lineage SARS-CoV-2 virus. Since the appearance of the Omicron lineage, Omicron subvariants have evolved, co-circulated, recombined and replaced each other locally or globally. Following the first dominant Omicron subvariants BA.1 and BA.2, BA.4 and BA.5 emerged with each displaying increasing levels of antibody escape, through mutation of spike, threatening vaccine efficacy and increasing hospitalisations [1,2 3–14]. In addition, Omicron subvariants are accumulating mutations across several of the genome, consistent with ongoing adaptation to host.

44 To understand phenotypic differences between Omicron subvariants, and the selective
45 forces driving their evolution, we compared replication of, and host responses to, BA.1-BA.5 with
46 Delta, the previously dominant VOC, in Calu-3 human airway epithelial cells (Fig. 1). We
47 equalized input dose of each variant by viral envelope (E) gene copies (RT-qPCR) as this ensures
48 cells are exposed to equal starting amounts of viral RNA, which is the major viral PAMP activating
49 defensive host innate immune responses[15,16]. Most importantly, this approach normalizes dose
50 independently of variant-specific differences in cell tropism or entry routes (Fig. 1a, Extended
51 Data Fig. 1a,b)[17–19], which we and others have shown impact both titer determination and input
52 equalization by cell-line infectivity measurements such as TCID50 or plaque assay (Extended
53 Data Fig. 1d-f). Our approach is particularly relevant for comparing Omicron subvariants because
54 spike mutations have been shown to alter tropism, increasing cathepsin-dependent endosomal
55 entry and reducing dependence on cell surface TMPRSS2[17,18,20,21], irrespective of virion spike
56 cleavage efficiency (Extended Data Fig. 1c). Endosomal cathepsins or cell surface TMPRSS2 are
57 required to cleave spike prior to ACE2 mediated entry[22,23]. Indeed, in line with previously published
58 data[17,19] we have found that Omicron, particularly BA.5, has enhanced entry (cathepsin
59 dependent and E64d-sensitive) in TMPRSS2-negative cells such as Hela-ACE2 compared to
60 previous VOCs such as Delta, whereas entry into Calu-3 cells is largely TMPRSS2-dependent
61 (camostat-sensitive) (Extended Data Fig. 1a.b) resulting in striking cell-type specific differences
62 between variant titers by TCID50 (Extended Data Fig. 1f).

63 Infection of Calu-3 cells with 2000 E gene copies/cell (Fig. 1) or 200 E copies/cell
64 (Extended Data Fig. 2) gave comparable E RNA (RT-qPCR) at 2 hours post infection (hpi),
65 consistent with equal input doses (Fig. 1a and Extended Data Fig. 2i). E gene measurements
66 during infection revealed that Omicron isolates BA.1, BA.2, BA.4 and BA.5 replicated similarly,
67 lagging behind Delta in Calu-3 cells (Fig. 1b, Extended Data Fig. 1k-n and Extended Data Fig.
68 2h). BA.4 replicated most slowly initially but caught up with BA.1, BA.2 and BA.5 by 24 hpi (Fig.

69 1b, Extended Data Fig. 1 and Extended Data Fig. 2h). Importantly, these replication differences
70 were observed consistently across several experiments (Fig. 1, Extended Data Fig. 1 and
71 Extended Data Fig. 2). As E gene measurement during infection captures gRNA as well as E, S
72 and Orf3 sgRNAs, we compared the levels of intracellular E RNA with those of Nsp12 and Orf1a
73 (Compare Extended Data Fig. 1k-l to Fig. 1b and Extended Data Fig. 1m-n to Extended Data Fig.
74 2h), which are uniquely encoded within gRNA. Importantly, the ratio of E to Nsp12 was similar
75 until 24hpi reflecting equivalent levels of E sgRNA synthesis between variants (Extended Data
76 Fig. 1o). Quantification of released virions by measuring E and Nsp12 RNA copies in the
77 supernatant mirrored viral replication (Extended Data Fig 1g-i). Similar patterns of infection were
78 also seen when quantified by intracellular Nucleocapsid (N) staining (Fig. 1c and Extended Data
79 Fig. 2j).

80 We next compared the host innate immune response to Omicron subvariants during
81 infection of Calu-3 cells. All viral stocks were prepared in human gastrointestinal Caco-2 cells as
82 they are naturally permissive to SARS-CoV-2 replication but do not mount a strong innate
83 response to this infection[15,24]. We confirmed that viral stocks prepared in Caco-2 cells (the highest
84 viral inoculum for each variant was 2000 E copies/cell) did not contain measurable IFNβ and
85 negligible IFNλ1/3 (ELISA) (Extended Data Fig 1p,q), ensuring differences in innate immune
86 activation in Calu-3 infections were not a result of IFN carryover in the viral stocks.

87 Strikingly, we found that infection of Calu-3 cells with BA.4 and BA.5 resulted in significantly less
88 innate immune activation compared to BA.1/BA.2, evidenced by lower induction of Interferon-β
89 (*IFNB*) and interferon stimulated genes (ISGs) including inflammatory chemokine *CXCL10* and
90 *RSAD2*, *DDX58*, *IFIT1* and *IFIT2* (Fig. 1d and Extended Data Fig 2c,d,l,m) and a trend towards
91 reduced *MX1* and *MX2* expression (Fig. 1d). Reduced host responses to BA.4 and BA.5 infection
92 were also evident at the level of IFNβ and CXCL10 secretion (Fig.1e,f). Slower replication of BA.4
93 likely contributes in part to the lesser innate immune activation during Calu-3 infection, but BA.5

94 replication was similar to BA.1 and BA.2 and nonetheless induced significantly less innate
95 immune responses. Inhibition of IFN-mediated JAK/STAT signaling with ruxolitinib, evidenced by
96 the absence of ISG induction (Extended Data Fig. 2d,l), rescued BA.1 and BA.2 infection in Calu-
97 3 cells to a greater degree than BA.4 or BA.5 (Fig. 1g and Extended Data Fig. 2b,n), suggesting
98 that the greater induction of IFNβ by BA.1 and BA.2 reduced their infectivity. BA.1-5 showed
99 similar sensitivities to a range of IFN doses used to pre-treat Calu-3 cells (Extended Data Fig. 2e-
100 g). We therefore conclude that the differences in ruxolitinib sensitivity reflect differences in IFN
101 induction after Calu-3 infection and not differences in IFN sensitivity. Infecting Calu-3 cells with
102 lower virus input doses (200 E copies/cell) recapitulated our observation that Delta replicated
103 better than Omicron BA.1-BA.5 (Extended Data Fig. 2h-j), and we again saw reduced innate
104 immune activation by BA.4 and BA.5 compared to BA.1 and BA.2 (Extended Data Fig. 2l,m). At
105 this lower inoculum, BA.4 infectivity was also strongly rescued by ruxolitinib treatment consistent
106 with its slower replication being due to IFN induction (Extended Data Fig. 2k).

107 We next compared Omicron subvariant replication and host responses in primary human
108 airway epithelial (HAE) cultures, which better recapitulate the heterogenous polarized epithelial
109 layer of the respiratory tract. We have previously reported that HAEs reveal differences in VOC
110 replication that likely reflect host adaptation, which are not always apparent in highly-permissive
111 cell lines, such as Calu-3[16,25]. Concordantly, BA.5 viral replication was higher than BA.2 and BA.4
112 in differentiated primary bronchial HAEs at 72hpi, while apical viral release over time was
113 comparable (Fig. 1h,i). Despite BA.4 and BA.5 replicating similarly to parental BA.2 in HAEs, we
114 consistently observed reduced innate activation, measured by ISG induction, after BA.4 and BA.5
115 infection (*IFNB, CXCL10, IFIT1, IFIT2, DDX58* and *RSAD2*) (Fig. 1k). Inhibiting IFN signaling with
116 JAK-inhibitor ruxolitinib suppressed ISG induction (Fig. 1k) and rescued replication of BA.2 to a
117 greater degree than BA.4 and BA.5 (Fig. 1j). Altogether, data in Figure 1 suggest adaptation to

118 reduce innate immune activation between the earliest (BA.1, BA.2) and subsequent (BA.4, BA.5)
119 Omicron subvariants.

120 SARS-CoV-2, and other respiratory viruses, reportedly replicate more efficiently in nasal
121 and tracheal epithelial cells[26], in part due to reduced innate activation and interferon-
122 responsiveness at the lower temperatures of the upper airway[27–29]. To investigate whether lower
123 temperatures reveal further Omicron subvariant adaptation, we compared replication at 32˚C in
124 Calu-3 cells. We found BA1-5 all replicated less well than at 37˚C (Extended Data Fig. 3a,b)
125 whereas Delta replication was not as temperature-sensitive. As expected[28], innate immune
126 activation in response to infection, or to RNA sensing agonist poly(I:C), was largely abolished at
127 32˚C (measured by *IFNB* and *CXCL10* mRNA induction) (Extended Data Fig. 3c-e). At 37˚C, we
128 again observed lower innate activation for BA.4 and BA.5 compared to BA.1/BA.2. In HAE,
129 lowering the temperature to 32˚C did not impact viral replication to the same extent as in Calu-3
130 cells (Extended Data Fig. 3f). However, we observed reduced virus output in apical washes from
131 infected HAE cultures for all Omicron isolates (Extended Data Fig. 3g-i). Infected HAEs at 32˚C
132 also expressed significantly less *IFNB* and *CXCL10* (Extended Data Fig. 3j,k). Overall, our data
133 suggest that Omicron does not replicate better at 32˚C in lung epithelial cells even in the absence
134 of an innate immune response. However, it is possible that the intra-tissue temperature
135 throughout the airways remains closer to 37˚C than the exhaled breath temperature of 32˚C
136 suggests[30].

137 We next investigated the mechanism underlying differential innate immune activation by
138 Omicron subvariants. IRF3 and STAT1 are key transcription factors responding to intracellular
139 RNA sensing, exemplified here by poly(I:C) treatment (Extended Data Fig. 4a and Fig. 3w,x). We
140 and others have shown SARS-CoV-2 activates transcription factors IRF3 and STAT1 downstream
141 of RNA sensing [15,31]. Consistent with their reduced innate immune triggering, we found Omicron
142 BA.4 and BA.5 infection activated significantly less IRF3 phosphorylation than BA.2 infection (Fig.

143 2a-c). A similar trend was observed for STAT1 serine 727 phosphorylation which is essential for
144 full STAT1 transcriptional activity[32], but not upstream JAK1-dependent tyrosine 701-
145 phosphorylation (Fig. 2a,d-f). Reduction of STAT1-phosphorylation correlated with reduced
146 STAT1 nuclear translocation during BA.4 and BA.5 infection compared to BA.2, measured by
147 high-content single-cell immunofluorescence imaging of infected nucleocapsid-positive Calu-3
148 cells (Fig. 2g). These data suggest BA.4 and BA.5 more effectively prevent intracellular activation
149 of innate sensing pathways. We previously reported that SARS-CoV-2 VOC Alpha evolved
150 enhanced innate immune evasion by increasing expression of key innate antagonists Orf6, Orf9b
151 and N (Extended Data Fig. 4m), which manipulate host cell innate immune pathways[16]. To
152 investigate whether Omicron subvariants have also independently evolved enhanced innate
153 immune suppression through similar mechanisms during human adaptation, we measured viral
154 innate antagonist protein expression during infection. Strikingly, we found that BA.4, and
155 particularly BA.5, expressed higher levels of Orf6 and N compared to BA.1 and BA.2 (Fig. 2i-m
156 and Extended Data Fig. 4b-h,j), measured at 48hpi in Calu-3 cells when E RNA levels were
157 equivalent (Fig. 2h). Unlike previous VOCs[16,25], expression of innate immune antagonist Orf9b
158 was not detected for any Omicron isolate, possibly due to Omicron subvariants encoding lineage-
159 specific Orf9b mutations (P10S and ΔENA at positions 27-29) altering antibody binding and
160 precluding detection by immunoblot (Fig. 2r and Extended Data Fig. 4m). Importantly, Orf9b
161 remained readily detectable in Delta-infected cells (Fig. 2r). Upregulation of Orf6 and N
162 expression by BA.5 was validated using a second independent isolate (Extended Data Fig. 4j-l),
163 and was also evident in lysates from infected HAEs (Extended Data Fig. 4i). Blocking IFN
164 signaling with ruxolitinib rescued replication of all Omicron isolates as before (Fig. 1 and Extended
165 Data Fig. 2) and enhanced viral protein detection by immunoblot (Fig. 2i,r and Extended Data Fig.
166 4b). Importantly, higher levels of BA.4 and BA.5 Orf6 and N remained apparent after ruxolitinib
167 treatment (Fig. 2i,l,m). We previously showed enhanced levels of Orf6, N and Orf9b protein by
168 Alpha were associated with increased levels of the corresponding sgRNAs[16]. By contrast, BA.5

169 Orf6 and N sgRNA levels (normalized to genomic Orf1a) were not enhanced, and were only
170 slightly upregulated during BA.4 infection (Fig. 2n,o), particularly in comparison to Alpha
171 (Extended Data Fig. 4n-p). No differences were observed in S and Orf3a sgRNAs which served
172 as controls to rule out a general enhancement of sgRNA synthesis (Fig. 2p,q). Although Omicron
173 subvariants have synonymous and non-synonymous mutations in Orf6 and N, there are no
174 mutations that distinguish BA.4 and BA.5 from BA.1 and BA.2 that provide a simple explanation
175 for increased Orf6 or N protein levels, including in their transcriptional regulatory sequences (TRS)
176 (Fig. 1 and 2, Extended Data Table 1 and 2). Thus, we hypothesize that BA.4 and BA.5 have
177 either evolved independent, novel mechanisms to increase Orf6 and N protein levels, or that the
178 increase is mediated by changes elsewhere in the genome, which may impact viral translation or
179 protein stability. Further studies are required to pinpoint the adaptations regulating Orf6 and N
180 expression levels.

181 Orf6 is a multifunctional viral accessory protein that modulates expression of host and viral
182 proteins[33,34]. Orf6 selectively inhibits host nuclear transport to potently antagonize antiviral
183 responses during infection. To probe Orf6 mechanisms, and its contribution to enhanced
184 antagonism by the VOCs, we used reverse genetics to introduce two stop-codons into the Orf6
185 coding-sequence of both Alpha (Alpha ΔOrf6) and BA.5 (BA.5 ΔOrf6), which we confirmed
186 abolished Orf6 expression during infection (Fig. 3b,j). While Alpha ΔOrf6 replicated similarly to
187 parental wild type (WT) virus up to 24hpi (Fig. 3a,b), we observed enhanced *IFNB* and *CXCL10*
188 expression (Fig. 3d) and protein secretion (Extended Data Fig. 5b) during Alpha ΔOrf6 infection
189 of Calu-3 cells compared to WT virus. Moreover, increased IRF3 nuclear translocation was
190 evident after Alpha ΔOrf6 infection at 24hpi using single cell quantitative immunofluorescence
191 microscopy (Fig. 3c and Extended Data Fig. 5a). This suggests an important role for Orf6 in innate
192 immune antagonism[16,34,35] and is consistent with suppression of IRF3 nuclear transport in Orf6
193 overexpression studies[34–36]. The reduction in Alpha ΔOrf6 replication at 48hpi, and N and spike

194 protein expression at 24hpi, that was rescued by ruxolitinib treatment, is also consistent with
195 greater IFN mediated suppression of the Orf6 deletion mutant (Fig. 3b and Extended Data Fig.
196 5c).

197 Alpha ΔOrf6 also replicated less well than WT in HAE cells (Fig. 3e-g and Extended Data
198 Fig. 5d). *IFNB* and *CXCL10* gene induction, normalized to *GAPDH*, were similar after Alpha ΔOrf6
199 and WT infection (Fig. 3h), despite lower E RNA levels for Alpha ΔOrf6, consistent with increased
200 innate immune induction by the deletion virus. Importantly, Alpha ΔOrf6 was more sensitive to
201 ruxolitinib treatment than WT, consistent with the notion that increased IFN induction caused
202 reduced replication of Alpha ΔOrf6 (Fig. 3f,g). To address the role of Orf6 during BA.5 infection,
203 we compared replication of a BA.5 ΔOrf6 mutant with parental BA.5 WT virus. We also generated
204 the first example of a BA.5 mutant bearing the Orf6 D61L mutation found in BA.2 and BA.4, that
205 has been proposed to reduce Orf6 function[25,31] (Fig. 3i,j). Consistent with SARS-CoV-2 Alpha
206 ΔOrf6 results, BA.5 ΔOrf6 showed a replication defect at 48hpi compared to BA.5 WT, and
207 triggered significantly enhanced innate immune responses evidenced by enhanced *IFNB* and ISG
208 induction (Fig. 3i-l). Deletion of Orf6 in BA.5 also increased the degree of infection-induced IRF3
209 and STAT1 phosphorylation (Fig. 3m-r) and nuclear translocation (Fig. 3s,t). This demonstrates
210 that Orf6 loss enhances IRF3 and STAT1 activation despite similar levels of infection, confirming
211 the important role of Orf6 in innate immune suppression and in distinguishing BA.5 from earlier
212 Omicron subvariants. Infection of HAEs confirmed reduced viral replication of the BA.5 ΔOrf6
213 compared to WT BA.5, while viral release remained comparable (Fig 3u,v and Extended Data
214 Fig. 5e). ISG expression in HAEs was similar between WT and mutant despite lower E RNA levels
215 during BA.5 ΔOrf6 infection, suggesting greater induction of innate immunity in the absence of
216 Orf6 in these cells (Extended Data Fig. 5f). Interestingly, introducing the C-terminal D61L mutation
217 into BA.5 Orf6 resulted in an intermediate innate immune phenotype measured by increased
218 induction of *IFNB*, *CXCL10* and *IFIT1* expression by the mutant virus (Fig. 3l). IRF3-

219 phosphorylation and translocation were equivalent between BA.5 WT and Orf6 D61L (Fig 3n-s),
220 whereas STAT1 translocation was not antagonized by Orf6 D61L (Fig. 3t), in line with reports of
221 a partial loss of Orf6-function in the D61L mutation[25,31]. These data suggest complex adaptation
222 of Orf6 manipulation of innate immunity during SARS-CoV-2 Omicron lineage adaptation.

223 During the course of this study, SARS-CoV-2 has continued to evolve and produce new
224 Omicron subvariants (Fig. 4a and Extended Data Fig. 6a). Omicron subvariants BA.2.75, XBB.1,
225 XBB.1.5 and BQ.1.1 have acquired increased ACE2 binding and enhanced adaptive immune
226 evasion[37 38–40]. To test whether enhanced innate immune antagonism is consistently associated
227 with globally successful subvariants, we compared BA.2.75, XBB.1, XBB.1.5 and BQ.1.1 isolates
228 to BA.2 and BA.5 (Fig. 4). We equalized virus dose by Nsp12 RNA copies (RT-qPCR), a
229 measurement of genomic RNA, rather than E RNA copies, due to accumulation of mutations in
230 the E gene of later Omicron subvariants, including in the region detected by our RT-qPCR assay.
231 We found that all Omicron subvariants retained an enhanced dependence on cathepsin, here
232 measured in A549 cells expressing ACE2 and TMPRSS2 (Extended Data Fig. 6b). BA.2.75,
233 XBB.1 (two independent isolates) and XBB.1.5, derived from the parental BA.2 lineage[38,40],
234 replicated comparably to earlier BA.2 and BA.5 in Calu-3 and HAEs (Fig. 4b-e and Extended Data
235 Fig. 6c-i). BQ.1.1, which has arisen from BA.5[40], displayed some reduction of replication in
236 epithelial cells (Fig. 4d,e,h and Extended Data Fig. 6e,f,i). Similar to BA.5, we found that all
237 subsequent Omicron subvariants tested triggered significantly less *IFNB* and *CXCL10* expression
238 than BA.2 at 24hpi (Fig. 4f,g). All Omicron subvariants derived from BA.2 (BA.2.75, XBB.1 and
239 XBB.1.5) showed reduced rescue by ruxolitinib treatment, as well as reduced induction of or
240 sensitivity to IFN, similar to BA.5 (Fig. 4h and Extended Data Fig. 6f). Strikingly, like BA.5,
241 enhanced innate immune evasion by these more recent subvariants was accompanied by
242 increased Orf6 expression for the majority of isolates (Fig. 4i,j). Reduced BQ.1.1 replication in
243 Calu-3 cells (Fig. 4d and Extended Data Fig. 6e) prevented Orf6 and N detection in the absence

244 of ruxolitinib (Fig. 4i). Reduced innate activation by recent Omicron subvariants also correlated
245 with reduced IRF3-phosphorylation compared to BA.2, and reduction of STAT1 serine-
246 phosphorylation was principally observed for XBB.1 and XBB.1.5 variants (Fig. 4k-m and
247 Extended Data Fig. 6j-l). Together these data are consistent with a trend for ongoing Omicron
248 evolution enhancing Orf6 expression as it adapts to the human population leading to reduced
249 innate immune responses, detectable at the level of IFN and ISG expression, and at the level of
250 transcription factor phosphorylation and nuclear translocation. This study considering Omicron
251 variants is very reminiscent of our previous observation of enhanced expression of key innate
252 immune antagonists Orf6, N and Orf9b in VOCs Alpha to Delta suggesting a common evolutionary
253 trajectory to combating human innate immunity and enhancing transmission[16,25].

254 We propose a model in which the earliest host innate immune responses make an
255 important contribution to SARS-CoV-2 transmission by influencing whether interactions with the
256 first few cells in the airway establish a productive infection. In this model, viruses with enhanced
257 ability to evade or antagonize innate immunity, for example through increased Orf6 and N
258 expression, will transmit with greater frequency because they are better at avoiding inducing, or
259 better at shutting down host responses that suppress this earliest replication.

260 How early viral manipulation of the host innate immune response influences disease is
261 less clear. We hypothesize that once infection of the airway is irrevocably established, innate
262 immune suppression that permits greater levels of viral replication may in turn lead to increased
263 disease, simply due to greater viral burden and greater inflammatory responses. This model is
264 supported by longitudinal nasal sampling of SARS-CoV-2 infected patients shortly after
265 confirmation of infection, which revealed pronounced and early upregulation of an innate immune
266 response in epithelial cells that rapidly declines after symptom onset [41]. Concordantly, higher
267 baseline antiviral gene expression and more potent innate induction in the nasal epithelium of
268 children are associated with less severe infection outcomes compared to adults[42]. Like others, we

269 assume this is explained by reduced viral loads reducing disease and early IFN protecting against
270 transmission, with late IFN responses contributing to disease[43]. Similarly, inborn errors of innate
271 antiviral mechanisms and IFN autoantibodies are associated with severe COVID19[44–48], assumed
272 to be explained by greater viral loads driving increased inflammatory disease. Furthermore,
273 clinical trials of JAK/STAT inhibitors reduced COVID-19 mortality after hospitalization[49].
274 Considering an unrelated virus, simian immunodeficiency virus (SIV) in macaques, may be
275 relevant. Here transmission efficiency and subsequent disease are also influenced by IFN at the
276 site of infection[50]. In all these examples, early IFN is beneficial, reducing transmission, but late
277 IFN is bad, increasing symptoms. Human SARS-CoV-2 challenge studies are expected to help
278 us understand the effect of these dynamics and innate immune contributions to transmission and
279 disease by permitting sampling before exposure and during the earliest time points post infection
280 with careful assessment of disease in a highly controlled environment[51,52].

281 We have focused on changes in expression of N and Orf6 but we expect that other viral
282 genes contribute to evasion of innate immunity and adaptation to humans. In contrast to common
283 cold coronaviruses, SARS-CoV-2 and its relatives encode a broad range of accessory genes[53,54]
284 which antagonize innate immunity and likely contribute to effective transmission between species.
285 Our data suggest that upregulation of Orf6 expression is a central feature of SARS-CoV-2
286 adaptation to humans. Our observations using Orf6-deletion viruses confirm Orf6 to be a potent
287 viral innate immune antagonist and are consistent with a model in which, like Alpha, Omicron
288 subvariant enhancement of Orf6 expression contributes to the reduced innate immune response
289 to infection compared earlier Omicron viruses. Orf6 upregulation by BA.5 may, in part, explain
290 increased pathogenicity *in vivo*[1,2]. This notion is supported by ∆Orf6 SARS-CoV-2 infection of
291 transgenic mice or hamsters, where the Orf6 mutant causes less severe disease and there is
292 quicker recovery from infection, despite comparable viral loads in nose and lungs[31,55]. Expression
293 of accessory and structural proteins as subgenomic RNAs during SARS-CoV-2 replication

294 provides an elegant mechanism to selectively regulate their abundance during adaptation to host,
295 as the level of each sgRNA and thus protein can be independently adjusted by mutation, as we
296 found for VOCs Alpha to Delta[16,25].

297 The earliest Omicron subvariants BA.1 and BA.2 outcompeted Delta despite not
298 enhancing innate immune antagonism, explained by extensive antibody escape and improved
299 spike function/stability[56,57]. This suggests adaptive immunity was the strongest selection force for
300 Omicron emergence and global dominance. We hypothesize that the acquisition of enhanced
301 innate immune suppression by Omicron lineage variants after their initial emergence required
302 selection for improved transmission and dominance. Thus, innate immune escape may be the
303 second dominant selective force the virus experiences after escape from neutralizing antibodies
304 in a population with pre-existing immunity from prior infection and vaccination. We propose that
305 evolving to better manage host innate immunity for improved transmission is a central feature of
306 species-specific host-adaptation for all emerging viruses. Intriguingly, SARS-CoV-2 continues to
307 jump species barriers and has been detected infecting 34 different animal species so far
308 (https://vis.csh.ac.at/sars-ani/), illustrating its remarkable capacity to universally antagonize
309 species specific innate immune responses. SARS-CoV-2 will be a fantastic model to further
310 dissect species barriers to zoonotic spillovers and understand how viruses adapt to new species.

311 We propose that adaptation in spike and beyond also contributes to enhanced replication
312 in human cells[16,25]. This may be important for outpacing early innate responses during
313 transmission particularly in environments with a mix of permissive and non-permissive cells such
314 as the upper human airways in which ACE2 is only expressed on ciliated cells[58]. Indeed, we have
315 found that SARS-CoV-2 replicates more slowly in primary HAE cultures than in Calu-3 cells and
316 that HAEs better recapitulate VOC replication advantages[16,25]. Primary HAEs complement more
317 tractable monoculture models, such as Calu-3 that allow mechanistic studies. We propose that
318 linking VOC genotype to phenotype in multiple models will be essential for effective prediction of

319 novel variant behavior. Moreover, understanding how adaptive changes in spike leading to altered
320 viral tropism influence innate immune responses also warrants further study.

321 We propose that this study adds to the body of evidence for innate immunity as a key
322 barrier which must be overcome by all pandemic zoonotic viruses, particularly in the absence of
323 immune memory in an exposure-naive species. This has also been elegantly demonstrated
324 recently for influenza virus (IVA) where avian, but not human IVA, is efficiently restricted by human
325 BTN3A3[59], which like MX1[60], can be overcome by adaptation to the human host. Innate immune
326 evasion has also been linked to the single pandemic HIV-1 lineage[61]. Our findings herein have
327 broad implications for understanding zoonotic pathogen emergence because they reveal
328 molecular details of how SARS-CoV-2 Omicron subvariants have achieved dominance,
329 unexpectedly by increasing specific protein expression rather than adapting by protein coding
330 mutation. Crucially, they suggest that improvements in innate immune evasion can continue to
331 enhance transmission, even after establishment in humans, illustrating an inevitable ongoing
332 trajectory of adaptation towards escape from the innate immune mechanisms that are the
333 gatekeepers of transmission success.

334

335 **Figure legends**

336 **Fig. 1. BA.5 displays enhanced innate immune antagonism during infection of airway**
337 **epithelial cells.**
338 (a-f) Calu-3 infection with 2000 E copies/cell of Delta (yellow; O), BA.1 (blue; O), BA.2 (blue; Δ),
339 BA.4 (purple; O) and BA.5 (purple; Δ), n=3. (**a**) Mean viral E copies at 2hpi across 3 independent
340 experiments at 2000 E copies/cell. (**b**) Viral replication over time measured by RT-qPCR for
341 intracellular E copies. (**c**) Infection levels measured by nucleocapsid expression (% N+ by flow
342 cytometry). (**d**) Expression of *IFNB*, *CXCL10*, *IFIT1, IFIT2, RSAD2, MX1, MX2* and *DDX58* in

343 infected cells over time. (**e**) IFNβ and (**f**) CXCL10 secretion from infected Calu-3 cells measured
344 by ELISA at 48hpi. (**g**) Rescue of viral replication by JAK1-inhibitor ruxolitinib in Calu-3 cells at
345 48hpi at 2000 E copies/cell. Shown are the relative infection levels across three independent
346 experiments determined by E copies/µg RNA normalized to the median infection level of the
347 untreated control. (h-k) Primary bronchial human airway epithelial cells (HAEs) were infected with
348 1500 E copies/cell of the indicated variants, n=3. Viral replication was measured by (**h**)
349 intracellular E copies at 72hpi and (**i**) viral release into apical washes over time. (**j**) Intracellular
350 viral E copies in HAEs in the presence or absence of ruxolitinib at 72hpi. (**k**) Expression of *IFNB*,
351 *CXCL10, IFIT1*, *IFIT2*, *DDX58* and *RSAD2* in cells from (j). Fold changes are normalized to mock
352 at (d) 2hpi or (k) 72hpi.
353 For statistical comparisons one-way ANOVA with Dunnett's post-test was used to compare all
354 variants at 2hpi in (a) or to compare BA.2 with other variants at 24 and 48hpi respectively (b-f).
355 Colors indicate comparator (Delta, yellow; BA.1, blue; BA.4, purple; BA.5, pink). For g and j,
356 indicated comparisons were performed using an unpaired one-tailed Student's t-Test. For h and
357 k, indicated comparisons were performed using one-way ANOVA with Dunnett's post-test. For i,
358 Two-way ANOVA with Bonferroni post-test were used to compare variants against BA.2. Mean+/-
359 SEM or individual datapoints are shown. hpi, hours post infection. *, $p<0.05$; **, $p<0.01$; ***,
360 $p<0.001$; n.s., not significant or exact p-value given (k).
361
362 **Fig. 2. BA.5 efficiently expresses SARS-CoV-2 innate antagonists during airway epithelial**
363 **cell infection.**
364 Calu-3 cells were infected with 2000 E copies/cell of the indicated variants. (**a**) Western blot of
365 STAT1-pY701, STAT1-pS727, total STAT1, IRF3-pS396, total IRF3, and β-Actin at 24hpi. (**b-f**)
366 Quantification of four independent western blots showing (**b**) P-IRF3, (**c**) IRF3, (**d**) STAT1-pS727
367 (**e**) STAT1-pY701 and (**f**) STAT1 over β-Actin at 24hpi. (**g**) Quantification of STAT1 translocation
368 detected by single-cell fluorescence microscopy over time in Calu-3 cells infected with the

369 indicated variants at 2000 E copies/cell. In infected cultures, translocation was determined in N+
370 cells. Data from 1500 cells/condition are shown. (**h**) Viral replication at 48hpi. (**i**) Representative
371 western blot of Orf6, N, spike/S2 and β-Actin at 48hpi in infected cells +/-5μM ruxolitinib. Non-
372 specific bands detected by polyclonal anti-spike primary antibody are indicated (see Extended
373 Data Fig. 2a for Mock). (**j-m**) Quantification of Orf6 and N expression from five independent
374 western blots of Calu-3 cells in the absence (**j**, Orf6; **k**, N) or presence of 5μM ruxolitinib (**l**, Orf6;
375 **m**, N), normalized to spike over BA.2. (**n-q**) sgRNA expression of (**n**) Orf6, (**o**) N, (**p**) spike and
376 (**q**) Orf3a normalized to Orf1a genomic RNA in Calu-3 cells at 48hpi, n=9. (**r**) Western blot of
377 Calu-3 cells infected with Delta, BA.1, BA.2, BA.4 and BA.5 at 2000 E copies/cell showing Orf9b,
378 Orf6, N and β-Actin expression at 48hpi+5μM ruxolitinib.
379 For b-f, h, j-q, one-way ANOVA with Dunnett's post-test was used to compare BA.2 with other
380 variants. For g Kruskal-Wallis test was used to compare groups at 24hpi and 48hpi. Mean+/-SEM
381 or individual datapoints are shown. hpi, hours post infection. sgRNA, subgenomic RNA. *, $p<0.05$;
382 ***, $p<0.001$; n.s., not significant.
383
384 **Fig. 3. Orf6 expression is a major determinant of enhanced innate immune antagonism by**
385 **emerging VOCs.**
386 (**a**) Replication of reverse genetic (RG) viruses parental Alpha WT and ΔOrf6 in Calu-3 cells
387 infected with 2000 E copies/cell over time, n=3. (**b**) Western blot of RG virus infections in Calu-3
388 cells at 24hpi for spike, N, Orf6 and β-Actin +/-5μM ruxolitinib. (**c**) Quantification of IRF3
389 translocation detected by single-cell fluorescence microscopy over time. In infected cultures,
390 translocation was determined in N+ cells. Data from 1500 cells/condition are shown. (**d**) *IFNB* and
391 *CXCL10* expression in cells from (a) over time, n=3. (**e-i**) Primary bronchial human airway
392 epithelial cells (HAEs) were infected with 1500 E copies/cell of the indicated variants in the
393 presence or absence of 5μM ruxolitinib, n=3. Viral replication was measured by (**e**) viral release
394 into apical washes over time. Replication measured by apical release in HAEs infected with (**f**)

395 Alpha WT or (**g**) ΔOrf6 in the presence or absence of 5μM ruxolitinib. (**h**) *IFNB* and *CXCL10*
396 expression in cells from (e). (**i**) Replication of RG viruses BA.5 WT, ΔOrf6 and Orf6 D61L isolates
397 in Calu-3 cells infected with 2000 E copies/cell over time. (**j**) Western blot of RG virus infections
398 in Calu-3 cells at 24hpi for spike, N, Orf6 and β-Actin. (**k**) *IFNB* expression in cells from (i) over
399 time. (**l**) Expression of *IFNB*, *CXCL10* and *IFIT1* in Calu-3 cells at 24hpi with 2000 E copies/cell
400 of the indicated viruses. (**m**) Western blot of STAT1-pY701, STAT1-pS727, total STAT1, IRF3-
401 pS396, total IRF3, and β-Actin at 24hpi. Quantification of four independent western blots showing
402 (**n**) IRF3-pS396, (**o**) total IRF3, (**p**) STAT1-pS727, (**q**) STAT1-pY701 and (**r**) total STAT1 over β-
403 Actin at 24hpi. Quantification of (**s**) IRF3 and (**t**) STAT1 translocation detected by single-cell
404 fluorescence microscopy over time. In infected cultures, translocation was determined in N+ cells.
405 Data from 1500 cells/condition are shown. (**u, v**) Replication of BA.5 WT and ΔOrf6 in HAEs
406 infected with 1500 E copies/cell in the (**u**) absence or (**v**) presence of 5μM ruxolitinib.
407 Quantification of (**w**) IRF3 and (**x**) STAT1 translocation detected by single-cell fluorescence
408 microscopy over time in Calu-3 cells stimulated with poly(I:C) or vehicle Lipofectamine2000 (L2K).
409 Data from 1500 cells/condition are shown.
410 For indicated statistical comparisons at each time point in a, d-l, m, o-s, v and w one-way ANOVA
411 with Dunnett's post-test was used. In c, x and y, groups were compared by Kruskal-Wallis test at
412 each time point. For j and l, RG mutants were compared to WT using a two-way ANOVA and
413 Bonferroni post-test. Colors indicate comparator (BA.5 ΔOrf6, purple; BA.5 Orf6 D61L, light pink).
414 Mean+/-SEM or individual datapoints are shown. hpi, hours post infection. *, $p<0.05$; **, $p<0.01$;
415 ***, $p<0.001$; n.s., not significant.
416
417 **Fig. 4. Innate immune phenotype of dominant Omicron subvariants.**
418 (**a**) Global SARS-CoV-2 variant sequence counts over time (scaled per variant), extracted from
419 CoV-Spectrum using genomic data from GISAID. (**b-d**) Calu-3 cells were infected with 2000
420 Nsp12 copies/cell. Replication of Omicron subvariants compared to BA.2 (blue) and BA.5 (purple)

421 measured by Nsp12 copies/µg RNA is shown for (**b**) BA.2.75 (yellow; O), (**c**) XBB-subvariants
422 (XBB.1: light red, O; XBB.1 (B): red, Δ; XBB.1.5: dark red, □) and (**d**) BQ.1.1 (BQ.1.1: light green,
423 O; BQ.1.1 (B): dark green, Δ) isolates. (**e**) HAEs were infected with 1500 Nsp12 copies/cell and
424 intracellular Nsp12 copies measured at 72hpi. (**f**) *IFNB* and (**g**) *CXCL10* expression in Calu-3
425 cells infected with 2000 Nsp12 copies/cell of the indicated Omicron subvariants at 24hpi. (**h**) Viral
426 replication of indicated variants in Calu-3 cells in the presence or absence of 5µM ruxolitinib at
427 48hpi. Numbers indicate fold change in replication in the presence of 5µM ruxolitinib. (**i,j**) Western
428 blot of Orf6, N, spike and β-Actin at 48hpi in infected Calu-3 cells from (b-d) in the (**i**) absence or
429 (**j**) presence of 5µM ruxolitinib. (**k**) Western blot of STAT1-pY701, STAT1-pS727, total STAT1,
430 IRF3-pS396, total IRF3, and β-Actin in Calu-3 cells at 24hpi. Quantification of two independent
431 western blots showing (**l**) IRF3-pS396 and (**m**) STAT1-pS727 over β-Actin at 24hpi.
432 For b-d, variant replication was compared to BA.2 at each time point using a two-way ANOVA
433 and Bonferroni post-test. Colors indicate comparator (BA.5, purple; BA.2.75, yellow; XBB.1, light
434 red; XBB.1 (B), red; XBB.1.5, dark red; BQ.1.1, light green; BQ.1.1 (B), dark green). For e-g, one-
435 way ANOVA with Dunnett's post-test was used to compare all variants to BA.2.
436 Mean+/-SEM or individual datapoints are shown. hpi, hours post infection. *, $p<0.05$; **, $p<0.01$;
437 ***, $p<0.001$; n.s., not significant.
438
439 **Extended Data Fig. 1. Replication measurements of SARS-CoV-2 variants.**
440 (**a**) Calu-3 and (**b**) Hela-ACE2 cells were infected with 1000 E copies/cell of the indicated variants
441 in the presence of DMSO (-), 25µM E64d or 25µM camostat. Infection levels were measured at
442 24hpi by nucleocapsid expression (% N+ by flow cytometry), n=3. (**c**) Representative western blot
443 of spike and N in purified SARS-CoV-2 virions, n=2. (**d**) Quantification of viral stock used in Fig.
444 1 and 2 by TCID50/ml on Hea-ACE2 cells. (**e**) Ratio of TCID50/ml over E copies/ml for virus
445 stocks from (d). (**f**) TCID50/ml of indicated virus stocks measured on ACE2-Hela or Calu-3 cells.
446 (**g-i**) Calu-3 cells were infected with 2000 E copies/cell of the indicated variants. At 24hpi, cells

447 and culture supernatant were harvested to determine intracellular viral replication and virus
448 release. (**g**) Intracellular replication (Cell) and viral release (Supernatant) was determined by
449 quantification of E copies at 24hpi. (**h**) Correlation graph of intracellular E copies and virus
450 released into supernatant at 24hpi. (**i**) Correlation of Nsp12 and E gene copies in supernatants
451 from (g). (**j**) Correlation of Nsp12 and E copies in apical washes from HAEs infected with BA.2
452 (blue) or BA.5 (purple) (samples from Fig. 4). Calu-3 cells were infected with 2000 E copies/cell
453 and viral replication measured by (**k**) Nsp12 copies/µg RNA or (**l**) Orf1a gRNA/*GAPDH* in cells
454 from Fig. 1a. Viral replication measured by (**m**) Nsp12 copies/µg RNA or (**n**) Orf1a gRNA/*GAPDH*
455 in cells infected with 200 E copies/ml from Extended Data Fig. 2h. (**o**) E copies/Nsp12 copies ratio
456 in Calu-3 cells over time calculated from three independent experiments. (**p**) IFNβ and (**q**) IFNλ1/3
457 levels detected in SARS-CoV-2 variant inoculum prepared from virus stocks prepped in Caco-2
458 cells.
459 For statistical comparison in a, b, k-q, one-way ANOVA with a Bonferroni post-test was used. For
460 a, b, groups were compared to DMSO. For k-o, groups were compared to BA.2 and colors indicate
461 comparator (Delta, yellow; BA.1, blue; BA.4, purple; BA.5, pink). For f, groups were compared by
462 paired Student's t-Test. R^2 and p-values in h-j were calculated using simple linear regression.
463 Mean+/-SEM or individual datapoints are shown. hpi, hours post infection. gRNA, genomic RNA.
464 *, p<0.05; **, p<0.01; ***, p<0.001; n.s., not significant.
465
466 **Extended Data Fig. 2. BA.5 displays enhanced innate immune antagonism during infection**
467 **of airway epithelial cells.**
468 (**a-d**) Calu-3 infection with 2000 E copies/cell of BA.1 (blue; O), BA.2 (blue; Δ), BA.4 (purple; O)
469 and BA.5 (purple; Δ), n=3. (**a**) Viral replication over time, n=3. (**b**) Viral replication of indicated
470 variants in the presence or absence of 5µM ruxolitinib at 48hpi, n=3. (**c**) *IFNB*, *CXCL10*, *IFIT1,*
471 *IFIT2* and *RSAD2* expression at 24hpi, n=3. (**d**) Expression of *IFNB* and *CXCL10* in the presence
472 of ruxolitinib in cells from (c). (**e-g**) IFNβ-sensitivity of indicated variants during Calu-3 cell infection

473 at 2000 E copies/cell. (**e**) Infection levels measured by % N+ at 24hpi at the indicated
474 concentrations of IFNβ, n=6. (**f**) Infection levels in cells from (e) at 0ng/ml IFNβ, n=6. (**g**) Infection
475 levels from (e) normalized to 0ng/ml IFNβ for each variant, n=6. (**h-m**) Calu-3 infection with 200
476 E copies/cell of Delta (yellow; O), BA.1 (blue; O), BA.2 (blue; Δ), BA.4 (purple; O) and BA.5
477 (purple; Δ), n=3. (**h**) Viral replication over time measured by RT-qPCR for intracellular E copies.
478 (**i**) Viral E copies at 2hpi in cells from (h). (**j**) Infections levels measured by nucleocapsid
479 expression (% N+ by flow cytometry). (**k**) Viral replication of indicated variants in Calu-3 cells from
480 (a) in the presence or absence of 5μM ruxolitinib at 48hpi, n=3. (**l**) Expression of *IFNB* and
481 *CXCL10* in the presence of ruxolitinib in cells from (h). (**m**) Expression of *IFNB, CXCL10* and
482 *IFIT1* in infected cells at 24hpi in cells from (h). (**n**) Fluorescence microscopy of Calu-3 cells
483 infected at 2000 E copies/cell at 48hpi in the presence or absence of 5μM ruxolitinib. Percentage
484 infection quantified by dsRNA-positive cells is indicated per condition. Nucleocapsid, green;
485 dsRNA, red; Hoechst33342, blue. Representative images shown. Scale bar, 50μm.
486 For statistical comparisons, one-way ANOVA and Dunnett's post-test were used. Groups were
487 compared as indicated or with BA.2. For e, comparisons were made against 0ng/ml IFNβ for each
488 variant. Colors in a, g and h indicate comparator (Delta, yellow; BA.1, blue; BA.4, purple; BA.5,
489 pink). Mean+/-SEM or individual datapoints are shown. hpi, hours post infection. *, $p<0.05$; **,
490 $p<0.01$; ***, $p<0.001$; n.s., not significant.
491
492 **Extended Data Fig. 3. Entry and replication characteristics of Omicron subvariant BA.5.**
493 (**a-d**) Calu-3 cells were infected with 2000 E copies/cell at 37ºC or 32ºC, n=3. (**a**) Viral replication
494 by RT-qPCR and (**b**) infection levels by flow cytometry at 24hpi. (**c**) *IFNB* and (**d**) *CXCL10*
495 expression in cells from (a). (**e**) *IFNB* and *CXCL10* expression in response to poly(I:C) transfection
496 in Calu-3 cells at 24h of stimulation, n=2. (**f-k**) Primary bronchial human airway epithelial cells
497 (HAEs) were infected with 1500 E copies/cell of the indicated variants at 37ºC or 32ºC, n=3. Viral
498 replication was measured by (**f**) intracellular E copies at 72hpi and viral release of (**g**) BA.2, (**h**)

499 BA.4 and (**i**) BA.5 into apical washes over time. Relative expression of (**j**) *IFNB* and (**k**) *CXCL10*
500 normalized to *GAPDH* in cells from (f). Fold changes are normalized to mock.
501 Pairwise comparisons were performed using an unpaired two-tailed Student's t-Test as indicated.
502 For g-i, two-way ANOVA with a Bonferroni post test was used to compare temperatures at each
503 time point. Mean+/-SEM or individual datapoints are shown. hpi, hours post infection. *, $p<0.05$;
504 **, $p<0.01$; ***, $p<0.001$; n.s., not significant or exact p-value given (k).
505
506 **Extended Data Fig. 4. BA.5 efficiently expresses SARS-CoV-2 innate antagonists during**
507 **airway epithelial cell infection.**
508 (**a**) Western blot of Calu-3 cells treated with poly(I:C), vehicle control lipofectamin2000 (L2K) or
509 5μM ruxolitinib where indicated. STAT1-pY701, STAT1-pS727, total STAT1, IRF3-pS396, total
510 IRF3, and β-Actin are shown at indicated time points. (**b**) Western blot of Orf6, N, spike/S2 and
511 β-Actin at 48hpi in infected Calu-3 cells +/-5μM ruxolitinib. Non-specific bands detected by
512 polyclonal anti-spike primary antibody are indicated. (**c-h**) Quantification of viral protein
513 expression from five independent western blots of infected Calu-3 cells at 48hpi +/-5μM ruxolitinib.
514 (**c,d**) Orf6, (**e,f**) N and (**g**,**h**) spike were normalized to β-Actin over BA.2. (**i**) Western blot of Orf6
515 and N expression by HAEs infected with 1500 E copies/cell of BA.2 or BA.5 over time. (**j**) Western
516 blot of Orf6, N, spike and β-Actin at 48hpi in Calu-3 cells infected with BA.1, BA.2 and two
517 independent BA.5 isolates. (**k,l**) Calu-3 cells were infected with BA.1, BA.2 and two independent
518 BA.5 isolates and (**k**) replication measured over time. (**l**) Expression of *IFNB*, *CXCL10* and *IFIT1*
519 is shown at 24hpi in cells from (k). (**m**) Western blot of Orf9b, Orf6, spike and β-Actin at 24hpi in
520 Calu-3 cells infected with the indicated variants at 2000 E copies/cell. (**n**) Viral replication in Calu-
521 3 cells by RT-qPCR at 24hpi, n=3. (**o**) Orf6 and (**p**) N sgRNA expression in cells from (n), n=3.
522 For c-h, l, n-o, one-way ANOVA with Dunnett's post-test was used to compare BA.2 with other
523 variants. For k, two-way ANOVA with a Bonferroni post-test was used to compare variants with
524 BA.2 at each time point. Colors indicate comparator (BA.1, blue BA.5, purple; BA.5 (B), pink).

525 Mean+/-SEM or individual datapoints are shown. hpi, hours post infection. sgRNA, subgenomic
526 RNA. *, p<0.05; ***, p<0.001; n.s., not significant.
527
528 **Extended Data Fig. 5. Orf6 expression is a major determinant of enhanced innate immune**
529 **antagonism by emerging VOCs.**
530 (**a**) Quantification of IRF3 translocation in Calu-3 cells infected with Alpha WT and ΔOrf6 detected
531 by single-cell fluorescence microscopy over time. Data from 1500 cells/condition are shown. (**b**)
532 IFNβ and CXCL10 secretion from infected Calu-3 cells measured at 48hpi, n=2. (**c**) Viral
533 replication in the presence or absence of 5μM ruxolitinib at 48hpi in cells from (Fig. 3a). (**d**)
534 Primary bronchial human airway epithelial cells (HAEs) were infected with 1500 E copies/cell of
535 the indicated variants in the presence or absence of 5μM ruxolitinib, Intracellular E copies are
536 shown (n=3). Apical washes are shown in Fig. 3e-g. (**e, f**) Infection of HAEs with BA.5 WT or BA.5
537 ΔOrf6 with 1500 E copies/cell showing (**e**) viral release into apical washes over time or (**f**) *IFNB*
538 and *CXCL10* expression at 72hpi.
539 For a, Kruskal-Wallis test was used to compare groups to mock at each time point. In b-d, one-
540 way ANOVA with Dunnett's post-test was used to compare groups as indicated. For e, groups
541 were compared at each time point using a two-way ANOVA with a Bonferroni post-test. Groups
542 in f were compared by paired Student's t-Test. *, p<0.05; **, p<0.01; ***, p<0.001; n.s., not
543 significant.
544
545 **Extended Data Fig. 6. Innate immune phenotype of dominant Omicron subvariants.**
546 (**a**) Absolute global SARS-CoV-2 variant sequence counts over time, extracted from CoV-
547 Spectrum using genomic data from GISAID. (**b**) ACE2/TMPRSS2-A549 cells were infected with
548 2000 Nsp12 copies/cell of the indicated SARS-CoV-2 variants in the presence of DMSO, 25μM
549 E45d or 25μM camostat. Infection levels were determined by N-positivity at 24hpi. (**c-e**) SARS-
550 CoV-2 Omicron subvariants infection of Calu-3 cells determined by N-positivity over time for the

551 indicated subvariants in cells from Fig. 4b-d with (**c**) BA.2.75 (yellow; O), (**d**) XBB-subvariants
552 (XBB.1: light red, O; XBB.1 (B): red, Δ; XBB.1.5: dark red, □) and (**e**) BQ.1.1 (BQ.1.1: light green,
553 O; BQ.1.1 (B): dark green, Δ) isolates shown. (**f**) Infection levels of indicated variants in Calu-3
554 cells in the presence or absence of 5μM ruxolitinib at 48hpi in cells from Fig. 4h. (**g-i**) Primary
555 bronchial human airway epithelial cells (HAEs) were infected with 1500 E copies/cell of the
556 indicated variants. Viral replication was measured by viral release into apical washes over time in
557 cells from Fig. 4e. (**g**) BA.2.75, (**h**) XBB-subvariants and (**i**) BQ.1.1 isolates are shown compared
558 to BA.2 (blue) and BA.5 (purple). Quantification of two independent western blots showing (**j**)
559 STAT1-pY701, (**k**) total IRF3 and (**l**) total STAT1 over β-Actin at 24hpi.
560 For b, treatments were compared to DMSO for each variant using one-way ANOVA and Dunnett's
561 post-test. For c-i, variant infection levels were compared to BA.2 at each time point by two-way
562 ANOVA and Bonferroni post-test. Colors indicate comparator (BA.5, purple; BA.2.75, yellow;
563 XBB.1, light red; XBB.1 (B), red; XBB.1.5, dark red; BQ.1.1, light green; BQ.1.1 (B), dark green).
564 Mean+/-SEM or individual datapoints are shown. hpi, hours post infection. *, $p<0.05$; **, $p<0.01$;
565 ***, $p<0.001$; n.s., not significant.
566

567 **Extended Data Table 1. Orf6 mutations detected in the Omicron subvariants**

568

569 **Extended Data Table 2. Nucleocapsid (N) mutations detected in the Omicron subvariants**

570

571 ## Methods

572 **Cell culture**

573 Calu-3 cells were purchased from AddexBio (C0016001), Caco-2 cells were a kind gift from Dalan
574 Bailey (Pirbright Institute), Hela-ACE2 cells were a gift from James E Voss[62] and A459 cells
575 expressing ACE2 and TMPRSS2 were a kind gift from Massimo Palmarini [19].Cell lines were
576 cultured in Dulbecco's modified Eagle Medium (DMEM) supplemented with 10% heat-inactivated
577 FBS (Labtech) and 100U/ml penicillin/streptomycin. Cells were passaged at 80-90% confluence.
578 For infections, Calu-3 and Caco-2 cells were seeded at $2x10^5$ cells/ml and Hela-ACE2 cells at
579 $1x10^5$ cells/ml and grown to 60-80% confluence for experiments[15,16]. Primary normal (healthy)
580 bronchial epithelial (NHBE-A) cells from two independent donors were cultured for five to seven
581 passages and differentiated at an air-liquid interface as previously described[15]. After 21-24 days
582 of differentiation, cells were used in infection experiments.

583 **Viruses**

584 SARS-CoV-2 lineages Alpha (B.1.1.7), Delta (B.1.617.2)[18] and Omicron (lineage
585 B.1.1.529.1/BA.1, lineage B.1.1.529.2/BA.2, lineage BA.2.75 (BA.2.75.3) lineage BQ.1.1
586 (BQ.1.1.1), lineage XBB.1) isolates were a gift from Wendy Barclay (Imperial College London,
587 UK). Omicron BA.4 (lineage B.1.1.529.4), BA.5 (lineage B.1.1.529.5), BQ.1.1 (B) (BQ.1.1.15) and
588 lineage XBB.1.5 (XBB.1.5.13) were a gift from Alex Sigal and Khadija Khan (Africa Health
589 Research Institute, Durban, South Africa)[5,13]. SARS-CoV-2 BA.5 (B) (SARS-CoV-
590 2/Norway/20365/2022) was obtained from the Norwegian Institute of Public Health, Oslo, Norway.
591 Omicron isolate identity was confirmed by full genome sequencing and assigned by Nextclade
592 v.2.14.1 (https://clades.nextstrain.org)[63,64] . Alpha Orf6 deletion virus (Alpha ΔOrf6) was achieved
593 by mutation of the first two methionines: M1L (A27216T) and M19L (A27200T). Reverse genetics
594 derived viruses were generated as previously described[65,66]. In brief, to generate the WT SARS-
595 CoV-2 Alpha variant, a set of overlapping viral genomic cDNA fragments were chemically
596 synthesized (GENEWIZ, Germany). The cDNA fragment representing the 5' terminus of the viral
597 genome contained the bacteriophage T7 RNA polymerase promoter and the fragment

598 representing the 3' terminus contained the T7 RNA polymerase termination sequences. These
599 fragments were then assembled into a full-length Alpha cDNA genome using the Transformation-
600 Associated Recombination (TAR) in yeast method[65] . To generate the Alpha virus carrying the
601 ATG codon changes (M1L and M19L) in its Orf6 gene (to generate Alpha ΔOrf6), the relevant
602 cDNA fragments were chemically synthesized (Thermofisher, UK) and the mutant viral genome
603 assembled using TAR in yeast as described above. We similarly generated WT BA.5, BA.5 ΔOrf6
604 (carrying M1L and M19L changes), and BA.5 Orf6 D61L (generated by introducing the GAT→CTC
605 nucleotide change found in BA.2) using TAR in yeast except that the assembled cDNA genomes
606 were placed under the control of the human cytomegalovirus promoter and the relevant
607 termination sequences. The assembled WT and Orf6 null mutant genomes were transfected into
608 BHK-hACE2-N cells stably expressing the SARS-CoV-2 N and the human ACE2 gene for virus
609 rescue[67]. The rescued viruses were passaged once (P1 stock) in Vero.E6 cells and their full
610 genomes sequenced using Oxford Nanopore as previously described [68]. For Alpha and BA.5 the
611 RG-derived viruses are referred to as WT, ΔOrf6 or Orf6 D61L to differentiate them from the
612 clinically isolated viruses used in all other experiments. All viruses were propagated by infecting
613 Caco-2 cells in DMEM culture medium supplemented with 1% FBS and 100U/ml
614 penicillin/streptomycin at 37 °C as previously described[15,16]. Virus was collected at 72 hpi and
615 clarified by centrifugation at 2,100xg for 15 min at 4°C to remove any cellular debris. Virus stocks
616 were aliquoted and stored at −80 °C. Virus stocks were quantified by extracting RNA from 100 µl
617 of supernatant with 1 µg/ml carrier RNA using Qiagen RNeasy clean-up RNA protocol, before
618 measuring viral E RNA copies per ml by RT-qPCR[15,16]. For experiments including Omicron
619 subvariants XBB.1 and BQ.1.1, stocks and viral replication were quantified using Nsp12 RNA
620 copies due to accumulation of mutations in the E gene of these variants, including in the region
621 detected by our RT-qPCR assay. Virus titres were determined by TCID50 in Hela-ACE2 cells. 10^4
622 cells were seeded in 96-well plates in 100µl. The next day, seven 10-fold serial dilutions of each
623 virus stock or supernatant were prepared and 50 µl added to the cells in quadruplicate. Cytopathic

624 effect (CPE) was scored at 48-72hpi. TCID50 per ml was calculated using the Reed & Muench
625 method, and an Excel spreadsheet created by B. D. Lindenbach was used for calculating TCID50
626 per ml values[69].

627 To generate SARS-CoV-2 lineage frequency plots for BA.1, BA.2, BA.4, BA.5, BA.2.75, BQ.1.1,
628 XBB.1 and XBB.1.5 (Fig. 4a and Extended Data Fig. 6a), respective sequence counts were
629 extracted from CoV-Spectrum (cov-spectrum.org)[70] using genomic data from GSAID[71].

630 **Virus culture and infection**

631 For infections, inoculum was calculated using E copies per cell quantified by RT-qPCR. Cells
632 were inoculated with indicated variants for 2h at 37°C, subsequently washed with PBS and fresh
633 DMEM culture medium supplemented with 1% FBS and 100U/ml penicillin/streptomycin was
634 added. At the indicated time points, cells were collected for analysis. For primary HAE infections,
635 virus was added to the apical side for 2-3 h at 37°C. Supernatant was then removed and cells
636 were washed twice with PBS. All liquid was removed from the apical side and basal medium was
637 replaced with fresh Pneumacult ALI medium for the duration of the experiment. Virus release was
638 measured at the indicated time points by extracting viral RNA from apical PBS washes. For
639 poly(I:C) (Peprotech) stimulations, cells were transfected with poly(I:C) using lipofectamine2000
640 (InvitroGen) in Opti-Mem (Thermo) for the indicated times. For IFN-sensitivity assays, cells were
641 pre-treated with indicated concentrations or recombinant human IFNβ (Peprotech) for 18h before
642 infection. Cytokines were maintained throughout the experiment. For inhibition assays, cells were
643 pre-treated with 5 μM Ruxolitinib (Cambridge Bioscience), 25μM camostat (Apexbio), 25μM E64d
644 (Focus Biomolecules) or DMSO control for 2-3h before SARS-CoV-2 infection. Inhibitors were
645 maintained throughout the infection.

646 **RT-qPCR of host and viral gene expression in infected cells**

647 Infected cells were lysed in RLT (Qiagen) supplemented with 0.1% beta-mercaptoethanol
648 (Sigma). RNA extractions were performed according to the manufacturer's instructions using
649 RNeasy Micro Kits (Qiagen) including on-column DNAse I treatment (Qiagen). cDNA was
650 synthesized using SuperScript IV (Thermo) with random hexamer primers (Thermo). RT-qPCR
651 was performed using Fast SYBR Green Master Mix (Thermo) for host gene expression and
652 subgenomic RNA expression or TaqMan Master mix (Thermo Fisher Scientific) for viral RNA
653 quantification, and reactions were performed on the QuantStudio 5 Real-Time PCR systems
654 (Thermo Fisher Scientific). Viral E RNA copies were determined as described previously[15,16]. Viral
655 subgenomic RNAs were detected using the same forward primer against the leader sequence
656 paired with a sgRNA specific reverse primer[16,72,73]. Using the 2−ΔΔCt method, sgRNA levels were
657 normalized to GAPDH to account for differences in RNA loading and then normalized to the level
658 of Orf1a gRNA quantified in the same way for each variant to account for differences in the level
659 of infection. Host gene expression was determined using the 2−ΔΔCt method and normalized to
660 GAPDH expression. The following probes and primers were used:

661 *GAPDH* fw: 5'-ACATCGCTCAGACACCATG-3', rv: 5'-TGTAGTTGAGGTCAATGAAGGG-3';
662 *IFNB* fw: 5'-GCTTGGATTCCTACAAAGAAGCA-3', rv: 5'-ATAGATGGTCAATGCGGCGTC-3';
663 *CXCL10* fw: 5'-TGGCATTCAAGGAGTACCTC-3', rv: 5'-TTGTAGCAATGATCTCAACACG-3';
664 *IFIT1* fw: 5'-CCTCCTTGGGTTCGTCTACA-3', rv: 5'-GGCTGATATCTGGGTGCCTA-3'; *IFIT2* fw:
665 5′-CAGCTGAGAATTGCACTGCAA-3′, rv: 5′-CGTAGGCTGCTCTCCAAGGA-3′; *MX1* fw: 5′-
666 ATCCTGGGATTTTGGGGCTT-3′, rv: 5′-CCGCTTGTCGCTGGTGTCG-3′; *MX2* fw: 5'-
667 CAGCCACCACCAGGAAAC-3', rv 5'-TTCTGCTCGTACTGGCTGTACAG-3', *RSAD2* fw: 5′-
668 CTGTCCGCTGGAAAGTG-3′, rv: 5′-GCTTCTTCTACACCAACATCC-3′; *DDX58* fw: 5'-
669 CTGGACCCTACCTACATCCTG-3', rv: 5'-GGCATCCAAAAAGCCACGG-3'. SARS-CoV-2 E
670 Sarbeco fw: 5′- CGTTAATAGTTAATAGCGTACTTCTTTTTC-3′; SARS-CoV-2 E Sarbeco
671 Probe1: 5′-FAM-ACACTAGCCATCCTTACTGCGCTTCG-TAMRA-3′; SARS-CoV-2 E Sarbeco rv

672 5′-ATATTGCAGCAGTACGCACACA-3′; SARS-CoV-2 Nsp12 fw: 5'-
673 GAGTGAAATGGTCATGTGTGG-3'; SARS-CoV-2 Nsp12 rv: 5'-
674 CATTGGCCGTGACAGCTTGAC-3'; SARS-CoV-2 Nsp12 Probe: 5'-
675 CTCATCAGGAGATGCCACAACTGCTTATGCTAATAG-3';5′ Leader fw: 5'-
676 ACCAACCAACTTTCGATCTCTTGT-3'; Orf1a rv: 5'-CCTCCACGGAGTCTCCAAAG-3'; Orf6
677 rv:GAGGTTTATGATGTAATCAAGATTC; N rv: 5'-CCAGTTGAATCTGAGGGTCCAC-3'; Orf3a
678 rv: 5'-GCAGTAGCGCGAACAAAAT-3'. S rv: 5'-GTCAGGGTAATAAACACCACGTG-3'.

679 **Flow cytometry**

680 Adherent cells were trypsinized and fixed in 4% formaldehyde prior to intracellular staining for
681 SARS-CoV-2 nucleocapsid (N) protein. For N detection, cells were permeabilized for 15 min with
682 Intracellular Staining Perm Wash Buffer (BioLegend) and subsequently incubated with 1μg/ml
683 CR3009 SARS-CoV-2 cross-reactive antibody (a gift from Laura McCoy) for 30 min at room
684 temperature. Primary antibodies were detected by incubation with secondary Alexa Fluor 488-
685 Donkey-anti-Human IgG (Jackson Labs). All samples were acquired on a BD Fortessa X20 or
686 LSR II using BD FACSDiva software. Data was analyzed using FlowJo v10.6.2 (Tree Star).

687 **Cytokine secretion**

688 Secreted mediators were detected in cell culture supernatants by ELISA. IFNβ, IFNλ1/3 and
689 CXCL10 were measured using Human IFN-beta Quantikine ELISA Kit, Human IL-29/IL-28B (IFN-
690 lambda 1/3) DuoSet ELISA or Human CXCL10/IP-10 DuoSet ELISA reagents (biotechne R&D
691 systems) according to the manufacturer's instructions.

692 **Western blotting**

693 For detection of N, Orf6, Orf9b, spike and β-actin expression, whole-cell protein lysates were
694 extracted with RIPA buffer, and then separated by SDS–PAGE, transferred onto nitrocellulose

695 and blocked in PBS with 0.05% Tween 20 and 5% skimmed milk. Membranes were probed with
696 rabbit-anti-SARS spike (Invitrogen, PA1-411-1165), mouse-anti-SARS-CoV-2 spike (GeneTex
697 1A9), rabbit-anti-Orf6 (Abnova, PAB31757), rabbit-anti-Orf9b (ProSci, 9191), Cr3009 SARS-CoV
698 cross-reactive human-anti-N antibody (a gift from Laura McCoy, UCL), rabbit-anti-phospho-
699 STAT1 (Ser727) (CellSignaling, Cat # 9177), rabbit-anti-phospho STAT1 (Tyr 701) (CellSignaling,
700 Cat# 9167, clone 58D6), rabbit-anti-STAT1 (CellSignaling, Cat# 9172), anit-rabbit-IRF3
701 (CellSignaling, Cat# 4302), rabbit-anti-phospho IRF3 (CellSignaling, Cat# 29047, clone D6O1M)
702 and rabbit-anti-beta-actin (SIGMA), followed by IRDye 800CW or 680RD secondary antibodies
703 (Abcam, goat anti-rabbit, goat anti-mouse or goat anti-human). Blots were imaged using an
704 Odyssey Infrared Imager (LI-COR Biosciences) and analyzed with Image Studio Lite software.
705 For virion blots, live virus normalized by equal total E copies was purified across a 25% sucrose
706 cushion and concentrated by centrifugation (2h 16500xg, 4^0C).

707 **Immunofluorescence staining and image analysis**

708 Infected cells were fixed using 4% PFA/formaldehyde for 1h at room temperature and
709 subsequently washed with PBS. A blocking step was carried out for 35h at room temperature with
710 10% goat serum/1%BSA/0.001 Triton-TX100 in PBS. dsRNA and nucleocapsid detection were
711 performed by primary incubation with rabbit-anti-IRF3 antibody (sc-33641, Santa Cruz), rabbit-
712 anti-STAT-1 (D1K9Y, Abcam), mouse-anti-dsRNA (MABE1134, Millipore) and Cr3009 SARS-
713 CoV cross-reactive human-anti-N antibodies for 18h and washed thoroughly in PBS. Primary
714 antibodies detection occurred using secondary anti-rabbit-AlexaFluor-488. anti-mouse-
715 AlexaFluor-568 and anti-human-Alexa647 conjugates (Jackson ImmunoResearch) for 1h. All
716 cells were labeled with Hoechst33342 (H3570, Thermo Fisher). Images were acquired using the
717 WiScan® Hermes 7-Colour High-Content Imaging System (IDEA Bio-Medical, Rehovot, Israel) at
718 magnification 10X/0.4NA. Four channel automated acquisition was carried out sequentially.
719 Images were acquired across a well area density resulting in 31 FOV/well and ~20,000 cells.

720 Images were pre-processed by applying a batch rolling ball background correction in FIJI ImageJ
721 software package[74] prior to quantification. IRF3 and STAT1 translocation analysis was carried out
722 using the Athena Image analysis software (IDEA Bio-Medical, Rehovot, Israel) and data post-
723 processed in Python. For dsRNA, Infected cell populations were determined by thresholding of
724 populations with greater than 2 segmented dsRNA punctae. For transcription factor translocation
725 analysis, infected populations were determined by presence of segmented nucleocapsid signal
726 within the cell.

727 **Statistical analysis**

728 Statistical analysis was performed using GraphPad Prism9 and details of statistical test used are
729 indicated. Data shows mean +/- SEM with significant differences or exact p-values indicated in
730 the figures. Significance levels were defined as follows: *, $p < 0.05$; **, $p < 0.01$ and ***, $p < 0.001$.

731 **Data availability**

732 All data generated or analyzed during this study are included in this manuscript (and its
733 supplementary information files). No new algorithms were developed for this project.

734 **Acknowledgements**

735 This work was funded by Wellcome Investigator Awards 223065 to C.J. and 220863 to G.J.T.
736 G.J.T. and C.J. were also funded by MRC/UKRI G2P-UK National Virology consortium
737 (MR/W005611/1) and the UCL COVID-19 fund. R.R is supported by a Marie Skłodowska-Curie
738 Individual Fellowships no. 896014. P.B received funding from the European Research Council
739 (ERC-Stg no. 639429), the Rosetrees Trust (M362-F1; M553), the NIHR GOSH BRC and the CF
740 Trust (SRC006; SRC020). M.V.X.W. is supported by the NIHR Biomedical Research Centre at
741 UCLH and IDEA Bio-Medical. The work at the CVR was funded by G2P-UK National Virology
742 Consortium funded by the MRC (MR/W005611/1) and MRC grants (MC_UU12014/2 and

743 MC_UU_00034/9) and the Wellcome Trust (206369/Z/17/Z). We are grateful to Wendy Barclay
744 (Imperial College London, UK), Alex Sigal and Khadija Khan (AHRI, South Africa) and the
745 Norwegian Institute of Public Health for provision of virus isolates and Dalan Bailey, Laura McCoy
746 and James Voss for reagents. For the purpose of Open Access, the authors have applied a CC
747 BY public copyright license to any Author Accepted Manuscript version arising from this
748 submission.

749

750 **Author contributions**

751 Conceptualisation: A-K.R., L.G.T., G.J.T. and C.J.

752 Designed experiments: A-K.R, L.G.T. V.C., W.F., G.d.L., G.J.T. and C.J.

753 Performed experiments: A-K.R, L.G.T., M.X.V.W., D.M., G.D., N.B., V.C., W.F., and G.d.L

754 Analyzed data: A-K.R., L.G.T., M.X.V.W., G.J.T. and C.J.

755 Generated and provided reagents: R.R. W.F., G.de L., V.M.C., J.T., P.B., M.P. and A.H.P.

756 Manuscript preparation and editing: A-K.R, L.G.T., D.M., A.H.P., M.P., G.J.T. and C.J.

757 Coordination and supervision: P.B., M.P., A.H.P., G.J.T. and C.J.

758

759 **Competing interests**

760 The authors declare that they have no competing interests.

761

Correspondence and request for materials should be addressed to Ann-Kathrin Reuschl, Clare Jolly or Greg J. Towers.

References

1. Hansen, C. H. *et al.* Risk of reinfection, vaccine protection, and severity of infection with the BA.5 omicron subvariant: a nation-wide population-based study in Denmark. *Lancet Infect. Dis.* **23**, 167–176 (2023).
2. Wolter, N. *et al.* Early assessment of the clinical severity of the SARS-CoV-2 omicron variant in South Africa: a data linkage study. *Lancet* **399**, 437–446 (2022).
3. Viana, R. *et al.* Rapid epidemic expansion of the SARS-CoV-2 Omicron variant in southern Africa. *Nature* **603**, 679–686 (2022).
4. Pulliam, J. R. C. *et al.* Increased risk of SARS-CoV-2 reinfection associated with emergence of Omicron in South Africa. *Science* **376**, eabn4947 (2022).
5. Tegally, H. *et al.* Emergence of SARS-CoV-2 Omicron lineages BA.4 and BA.5 in South Africa. *Nat. Med.* **28**, 1785–1790 (2022).
6. Cao, Y. *et al.* BA.2.12.1, BA.4 and BA.5 escape antibodies elicited by Omicron infection. *Nature* **608**, 593–602 (2022).
7. Neutralization Escape by the SARS-CoV-2 Omicron Variants BA. 2.12. 1 and BA. 4/BA. 5 (preprint). https://pesquisa.bvsalud.org/global-literature-on-novel-coronavirus-2019-ncov/resource/pt/ppcovidwho-336957.
8. Gruell, H. *et al.* Delineating antibody escape from Omicron sublineages. *bioRxiv* 2022.04.06.487257 (2022) doi:10.1101/2022.04.06.487257.
9. Wang, Q. *et al.* Antibody evasion by SARS-CoV-2 Omicron subvariants BA.2.12.1, BA.4 and BA.5. *Nature* **608**, 603–608 (2022).

786 10. Tuekprakhon, A. *et al.* Antibody escape of SARS-CoV-2 Omicron BA.4 and BA.5 from
787 vaccine and BA.1 serum. *Cell* **185**, 2422–2433.e13 (2022).
788 11. Willett, B. J. *et al.* Distinct antigenic properties of the SARS-CoV-2 Omicron lineages BA.4
789 and BA.5. *bioRxiv* (2022) doi:10.1101/2022.05.25.493397.
790 12. Kimura, I. *et al.* Virological characteristics of the SARS-CoV-2 Omicron BA.2 subvariants,
791 including BA.4 and BA.5. *Cell* **185**, 3992–4007.e16 (2022).
792 13. Khan, K. *et al.* Omicron sub-lineages BA.4/BA.5 escape BA.1 infection elicited neutralizing
793 immunity. *bioRxiv* (2022) doi:10.1101/2022.04.29.22274477.
794 14. Steel, K., Fordham, E. & Bracher, M. Coronavirus (COVID-19) infection survey, UK - office
795 for national statistics.
796 https://www.ons.gov.uk/peoplepopulationandcommunity/healthandsocialcare/conditionsand
797 diseases/bulletins/coronaviruscovid19infectionsurveypilot/8july2022 (2022).
798 15. Thorne, L. G. *et al.* SARS-CoV-2 sensing by RIG-I and MDA5 links epithelial infection to
799 macrophage inflammation. *EMBO J.* **40**, e107826 (2021).
800 16. Thorne, L. G. *et al.* Evolution of enhanced innate immune evasion by SARS-CoV-2. *Nature*
801 **602**, 487–495 (2022).
802 17. Meng, B. *et al.* Altered TMPRSS2 usage by SARS-CoV-2 Omicron impacts infectivity and
803 fusogenicity. *Nature* **603**, 706–714 (2022).
804 18. Peacock, T. P. *et al.* The altered entry pathway and antigenic distance of the SARS-CoV-2
805 Omicron variant map to separate domains of spike protein. *bioRxiv* (2022)
806 doi:10.1101/2021.12.31.474653.
807 19. Willett, Grove & MacLean. SARS-CoV-2 Omicron is an immune escape variant 253 with an
808 altered cell entry pathway. *Nat. Microbiol.*
809 20. Willett, B. J. *et al.* The hyper-transmissible SARS-CoV-2 Omicron variant exhibits
810 significant antigenic change, vaccine escape and a switch in cell entry mechanism. *bioRxiv*
811 (2022) doi:10.1101/2022.01.03.21268111.

812 21. Mesner, D. *et al.* SARS-CoV-2 evolution influences GBP and IFITM sensitivity. *Proc. Natl.*
813 *Acad. Sci. U. S. A.* **120**, e2212577120 (2023).
814 22. Hoffmann, M., Kleine-Weber, H. & Pöhlmann, S. A Multibasic Cleavage Site in the Spike
815 Protein of SARS-CoV-2 Is Essential for Infection of Human Lung Cells. *Mol. Cell* **78**, 779–
816 784.e5 (2020).
817 23. Hoffmann, M. *et al.* SARS-CoV-2 Cell Entry Depends on ACE2 and TMPRSS2 and Is
818 Blocked by a Clinically Proven Protease Inhibitor. *Cell* **181**, 271–280.e8 (2020).
819 24. Stanifer, M. L. *et al.* Critical Role of Type III Interferon in Controlling SARS-CoV-2 Infection
820 in Human Intestinal Epithelial Cells. *Cell Rep.* **32**, 107863 (2020).
821 25. Bouhaddou, M. *et al.* Global landscape of the host response to SARS-CoV-2 variants
822 reveals viral evolutionary trajectories. *bioRxiv* 2022.10.19.512927 (2022)
823 doi:10.1101/2022.10.19.512927.
824 26. V'kovski, P. *et al.* Disparate temperature-dependent virus–host dynamics for SARS-CoV-2
825 and SARS-CoV in the human respiratory epithelium. *PLoS Biol.* **19**, e3001158 (2021).
826 27. Foxman, E. F., Storer, J. A., Vanaja, K., Levchenko, A. & Iwasaki, A. Two interferon-
827 independent double-stranded RNA-induced host defense strategies suppress the common
828 cold virus at warm temperature. *Proc. Natl. Acad. Sci. U. S. A.* **113**, 8496–8501 (2016).
829 28. Foxman, E. F. *et al.* Temperature-dependent innate defense against the common cold virus
830 limits viral replication at warm temperature in mouse airway cells. *Proc. Natl. Acad. Sci. U.*
831 *S. A.* **112**, 827–832 (2015).
832 29. Huang, D. *et al.* Cold exposure impairs extracellular vesicle swarm–mediated nasal antiviral
833 immunity. *J. Allergy Clin. Immunol.* **151**, 509–525.e8 (2023).
834 30. Khosravi, M. *et al.* A Distinct Difference Between Air and Mucosal Temperatures in Human
835 Respiratory Tract. *Front. Med.* **8**, 650637 (2021).
836 31. Kehrer, T. *et al.* Impact of SARS-CoV-2 ORF6 and its variant polymorphisms on host
837 responses and viral pathogenesis. *bioRxiv* (2022) doi:10.1101/2022.10.18.512708.

838 32. Sadzak, I., Schiff, M., Gattermeier, I., Glinitzer, R. & Sauer, I. Saalmü ller A, Yang E,
839 Schaljo B, Kovarik P. 2008. Recruitment of Stat1 to chromatin is required for interferon-
840 induced serine phosphorylation of Stat1 transactivation domain. *Proc. Natl. Acad. Sci. U. S.*
841 *A.* **105**, 8944–8949.
842 33. Kimura, I., Konno, Y., Sauter, D., Nakagawa, S. & Sato, K. Sarbecovirus ORF6 Proteins
843 Hamper the Induction of Interferon Signaling by Blocking mRNA Nuclear Export (preprint).
844 (2020).
845 34. Miorin, L. *et al.* SARS-CoV-2 Orf6 hijacks Nup98 to block STAT nuclear import and
846 antagonize interferon signaling. *Proc. Natl. Acad. Sci. U. S. A.* **117**, 28344–28354 (2020).
847 35. Lei, X. *et al.* Activation and evasion of type I interferon responses by SARS-CoV-2. *Nat.*
848 *Commun.* **11**, 3810 (2020).
849 36. Addetia, A. *et al.* SARS-CoV-2 ORF6 Disrupts Bidirectional Nucleocytoplasmic Transport
850 through Interactions with Rae1 and Nup98. mBio. 2021; 12: e00065--21.
851 37. Saito, A. *et al.* Virological characteristics of the SARS-CoV-2 Omicron BA.2.75 variant. *Cell*
852 *Host Microbe* **30**, 1540–1555.e15 (2022).
853 38. Tamura, T. *et al.* Virological characteristics of the SARS-CoV-2 XBB variant derived from
854 recombination of two Omicron subvariants. *Nat. Commun.* **14**, 2800 (2023).
855 39. Uriu, K. *et al.* Enhanced transmissibility, infectivity, and immune resistance of the SARS-
856 CoV-2 omicron XBB.1.5 variant. *Lancet Infect. Dis.* **23**, 280–281 (2023).
857 40. Ito, J. *et al.* Convergent evolution of SARS-CoV-2 Omicron subvariants leading to the
858 emergence of BQ.1.1 variant. *Nat. Commun.* **14**, 2671 (2023).
859 41. Loske, J. *et al.* Pre-activated antiviral innate immunity in the upper airways controls early
860 SARS-CoV-2 infection in children. *Nat. Biotechnol.* **40**, 319–324 (2022).
861 42. Cheemarla, N. R. *et al.* Dynamic innate immune response determines susceptibility to
862 SARS-CoV-2 infection and early replication kinetics. *J. Exp. Med.* **218**, (2021).
863 43. Park, A. & Iwasaki, A. Type I and type III interferons--induction, signaling, evasion, and

application to combat COVID-19. *Cell Host Microbe* **27**, 870–878 (2020).

44. Zhang, Q. *et al.* Inborn errors of type I IFN immunity in patients with life-threatening COVID-19. *Science* **370**, (2020).
45. Bastard, P. *et al.* Autoantibodies against type I IFNs in patients with life-threatening COVID-19. *Science* **370**, (2020).
46. Pairo-Castineira, E. *et al.* Genetic mechanisms of critical illness in COVID-19. *Nature* **591**, 92–98 (2021).
47. Zhang, Q., Bastard, P., COVID Human Genetic Effort, Cobat, A. & Casanova, J.-L. Human genetic and immunological determinants of critical COVID-19 pneumonia. *Nature* **603**, 587–598 (2022).
48. Wickenhagen, A. *et al.* A prenylated dsRNA sensor protects against severe COVID-19. *Science* **374**, eabj3624 (2021).
49. Selvaraj, V., Finn, A., Lal, A. & Carino, G. P. BARICITINIB IN HOSPITALIZED PATIENTS WITH COVID-19: META-ANALYSIS OF RANDOMIZED CONTROLLED TRIALS. *Chest* **162**, A972 (2022).
50. Sandler, N. G. *et al.* Type I interferon responses in rhesus macaques prevent SIV infection and slow disease progression. *Nature* **511**, 601–605 (2014).
51. Killingley, B. *et al.* Safety, tolerability and viral kinetics during SARS-CoV-2 human challenge in young adults. *Nat. Med.* **28**, 1031–1041 (2022).
52. Rosenheim, J. *et al.* SARS-CoV-2 human challenge reveals single-gene blood transcriptional biomarkers that discriminate early and late phases of acute respiratory viral infections. *bioRxiv* (2023) doi:10.1101/2023.06.01.23290819.
53. Brant, A. C., Tian, W., Majerciak, V., Yang, W. & Zheng, Z.-M. SARS-CoV-2: from its discovery to genome structure, transcription, and replication. *Cell Biosci.* **11**, 136 (2021).
54. Pagani, I., Ghezzi, S., Alberti, S., Poli, G. & Vicenzi, E. Origin and evolution of SARS-CoV-2. *Eur Phys J Plus* **138**, 157 (2023).

890 55. Silvas, J. A. *et al.* Contribution of SARS-CoV-2 Accessory Proteins to Viral Pathogenicity in
891 K18 Human ACE2 Transgenic Mice. *J. Virol.* (2021) doi:10.1128/jvi.00402-21.
892 56. Chin, A. W. H., Lai, A. M. Y., Peiris, M. & Poon, L. L. M. SARS-CoV-2 Omicron variant is
893 more stable than the ancestral strain on various surfaces. *bioRxiv* 2022.03.09.483703
894 (2022) doi:10.1101/2022.03.09.483703.
895 57. Hirose, R. *et al.* Differences in environmental stability among SARS-CoV-2 variants of
896 concern: Omicron has higher stability. *bioRxiv* 2022.01.18.476607 (2022)
897 doi:10.1101/2022.01.18.476607.
898 58. Lee, I. T. *et al.* ACE2 localizes to the respiratory cilia and is not increased by ACE inhibitors
899 or ARBs. *Nat. Commun.* **11**, 1–14 (2020).
900 59. Pinto, R. M. *et al.* BTN3A3 evasion promotes the zoonotic potential of influenza A viruses.
901 *Nature* **619**, 338–347 (2023).
902 60. Riegger, D. *et al.* The Nucleoprotein of Newly Emerged H7N9 Influenza A Virus Harbors a
903 Unique Motif Conferring Resistance to Antiviral Human MxA. *J. Virol.* (2014)
904 doi:10.1128/jvi.02406-14.
905 61. Zuliani-Alvarez, L. *et al.* Evasion of cGAS and TRIM5 defines pandemic HIV. *Nature*
906 *Microbiology* **7**, 1762–1776 (2022).
907 62. Rogers, T. F. *et al.* Isolation of potent SARS-CoV-2 neutralizing antibodies and protection
908 from disease in a small animal model. *Science* **369**, 956–963 (2020).
909 63. Hadfield, J. *et al.* Nextstrain: real-time tracking of pathogen evolution. *Bioinformatics* **34**,
910 4121–4123 (2018).
911 64. Aksamentov, I., Roemer, C., Hodcroft, E. & Neher, R. Nextclade: clade assignment,
912 mutation calling and quality control for viral genomes. *J. Open Source Softw.* **6**, 3773
913 (2021).
914 65. Zhou, J. *et al.* Mutations that adapt SARS-CoV-2 to mink or ferret do not increase fitness in
915 the human airway. *Cell Rep.* **38**, 110344 (2022).

916 66. Thi Nhu Thao, T. *et al.* Rapid reconstruction of SARS-CoV-2 using a synthetic genomics
917 platform. *Nature* **582**, 561–565 (2020).
918 67. Rihn, S. J. *et al.* A plasmid DNA-launched SARS-CoV-2 reverse genetics system and
919 coronavirus toolkit for COVID-19 research. *PLoS Biol.* **19**, e3001091 (2021).
920 68. da Silva Filipe, A. *et al.* Genomic epidemiology reveals multiple introductions of SARS-CoV-
921 2 from mainland Europe into Scotland. *Nat Microbiol* **6**, 112–122 (2021).
922 69. Lindenbach, B. D. Measuring HCV Infectivity Produced in Cell Culture and In Vivo.
923 *Hepatitis C* 329–336 (2009).
924 70. Chen, C. *et al.* CoV-Spectrum: analysis of globally shared SARS-CoV-2 data to identify and
925 characterize new variants. *Bioinformatics* **38**, 1735–1737 (2022).
926 71. Elbe, S. & Buckland-Merrett, G. Data, disease and diplomacy: GISAID's innovative
927 contribution to global health. *Glob Chall* **1**, 33–46 (2017).
928 72. Parker, M. D. *et al.* Altered subgenomic RNA abundance provides unique insight into
929 SARS-CoV-2 B.1.1.7/Alpha variant infections. *Commun Biol* **5**, 666 (2022).
930 73. Meredith, L. W. *et al.* Rapid implementation of SARS-CoV-2 sequencing to investigate
931 cases of health-care associated COVID-19: a prospective genomic surveillance study.
932 *Lancet Infect. Dis.* **20**, 1263–1271 (2020).
933 74. Schindelin, J. *et al.* Fiji: an open-source platform for biological-image analysis. *Nat.*
934 *Methods* **9**, 676–682 (2012).

Figure 1

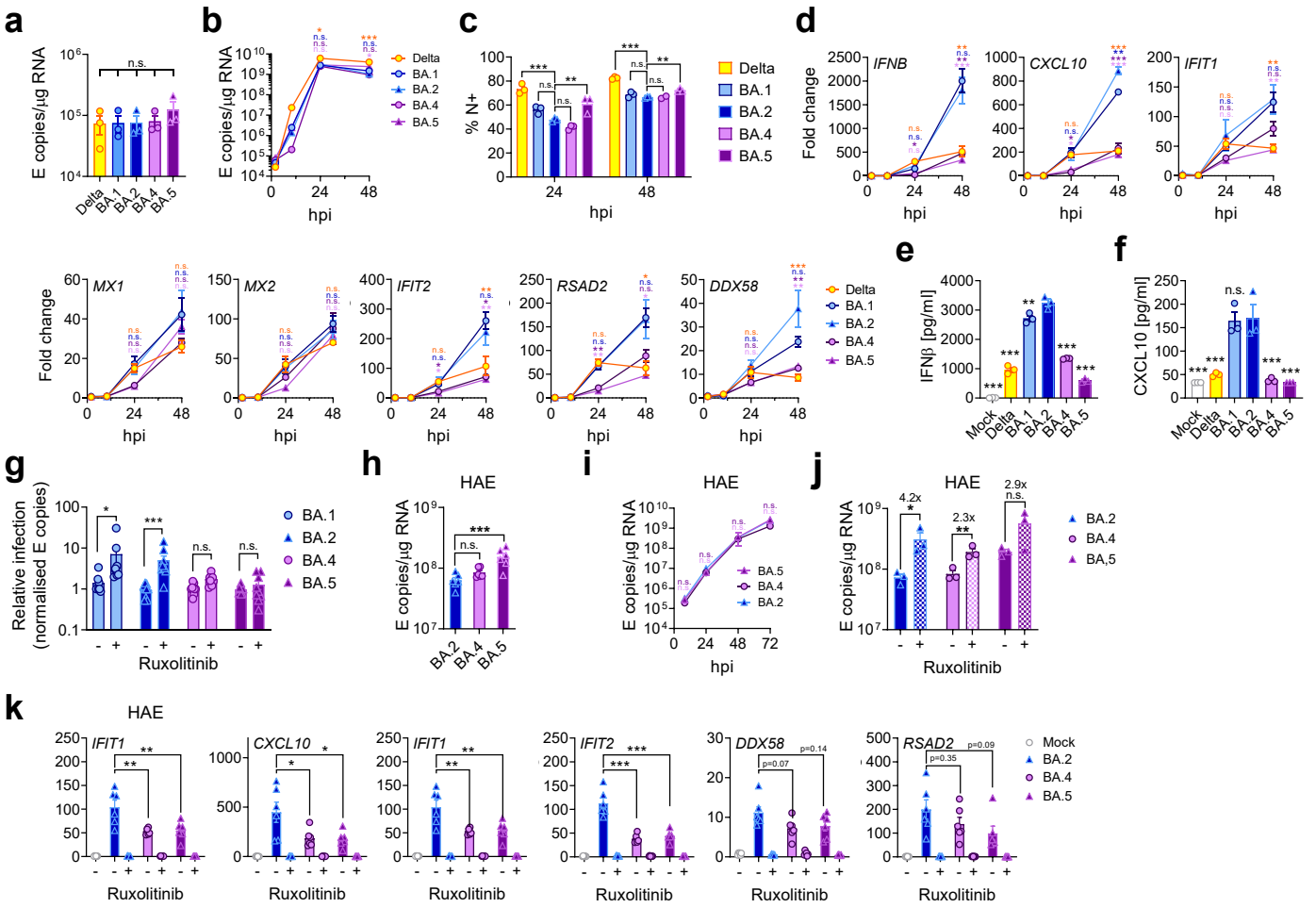

Fig. 1. BA.5 displays enhanced innate immune antagonism during infection of airway epithelial cells.
(a-f) Calu-3 infection with 2000 E copies/cell of Delta (yellow; O), BA.1 (blue; O), BA.2 (blue; Δ), BA.4 (purple; O) and BA.5 (purple; Δ), n=3. (**a**) Mean viral E copies at 2hpi across 3 independent experiments at 2000 E copies/cell. (**b**) Viral replication over time measured by RT-qPCR for intracellular E copies. (**c**) Infection levels measured by nucleocapsid expression (% N+ by flow cytometry). (**d**) Expression of *IFNB*, *CXCL10*, *IFIT1, IFIT2, RSAD2, MX1, MX2* and *DDX58* in infected cells over time. (**e**) IFNβ and (**f**) CXCL10 secretion from infected Calu-3 cells measured by ELISA at 48hpi. (**g**) Rescue of viral replication by JAK1-inhibitor ruxolitinib in Calu-3 cells at 48hpi at 2000 E copies/cell. Shown are the relative infection levels across three independent experiments determined by E copies/µg RNA normalized to the median infection level of the untreated control. (h-k) Primary bronchial human airway epithelial cells (HAEs) were infected with 1500 E copies/cell of the indicated variants, n=3. Viral replication was measured by (**h**) intracellular E copies at 72hpi and (**i**) viral release into apical washes over time. (**j**) Intracellular viral E copies in HAEs in the presence or absence of ruxolitinib at 72hpi. (**k**) Expression of *IFNB*, *CXCL10, IFIT1*, *IFIT2*, *DDX58* and *RSAD2* in cells from (j). Fold changes are normalized to mock at (d) 2hpi or (k) 72hpi.
For statistical comparisons one-way ANOVA with Dunnett's post-test was used to compare all variants at 2hpi in (a) or to compare BA.2 with other variants at 24 and 48hpi respectively (b-f). Colors indicate comparator (Delta, yellow; BA.1, blue; BA.4, purple; BA.5, pink). For g and j, indicated comparisons were performed using an unpaired one-tailed Student's t-Test. For h and k, indicated comparisons were performed using one-way ANOVA with Dunnett's post-test. For i, Two-way ANOVA with Bonferroni post-test were used to compare variants against BA.2. Mean+/-SEM or individual datapoints are shown. hpi, hours post infection. *, p<0.05 ; **, p<0.01; ***, p<0.001; n.s., not significant or exact p-value given (k).

Figure 2

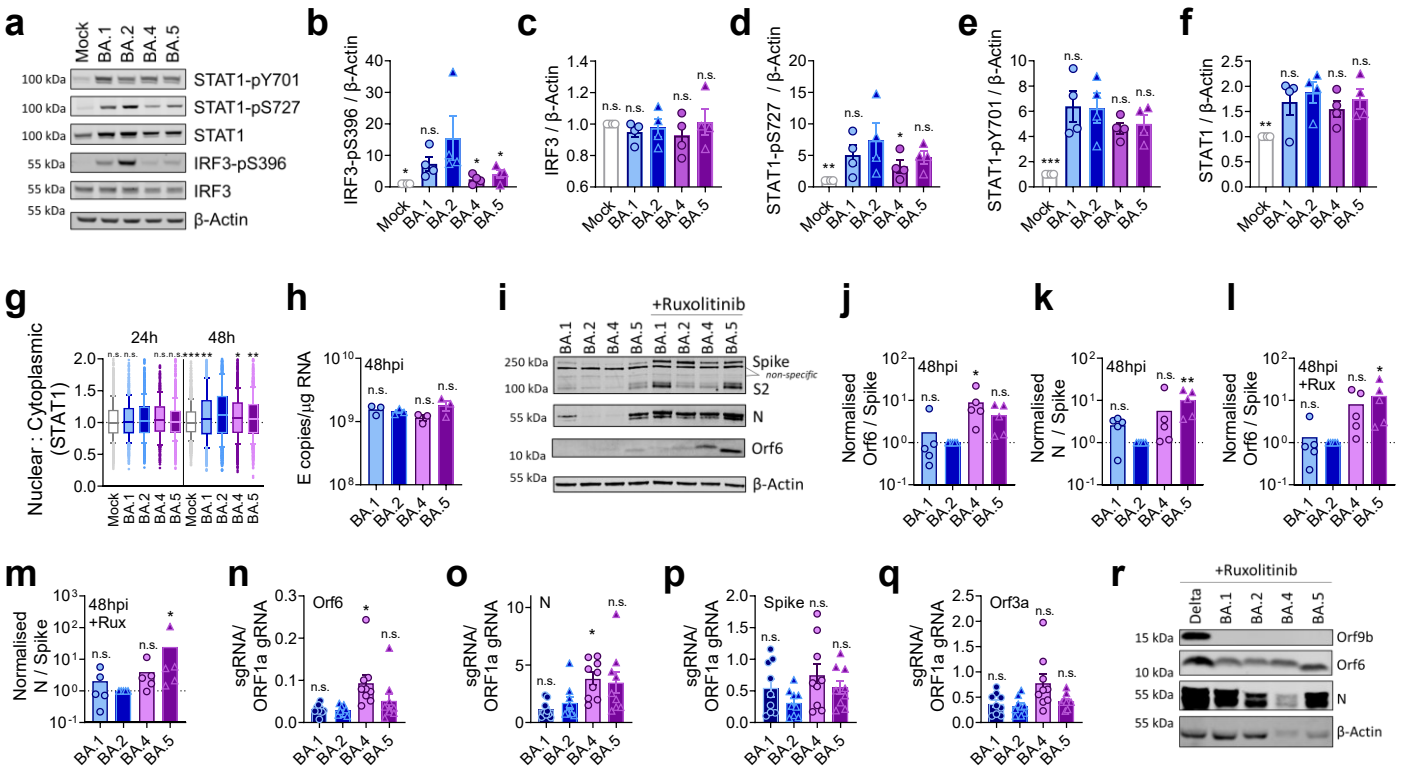

Fig. 2. BA.5 efficiently expresses SARS-CoV-2 innate antagonists during airway epithelial cell infection.
Calu-3 cells were infected with 2000 E copies/cell of the indicated variants. (**a**) Western blot of STAT1-pY701, STAT1-pS727, total STAT1, IRF3-pS396, total IRF3, and β-Actin at 24hpi. (**b-f**) Quantification of four independent western blots showing (**b**) P-IRF3, (**c**) IRF3, (**d**) STAT1-pS727 (**e**) STAT1-pY701 and (**f**) STAT1 over β-Actin at 24hpi. (**g**) Quantification of STAT1 translocation detected by single-cell fluorescence microscopy over time in Calu-3 cells infected with the indicated variants at 2000 E copies/cell. In infected cultures, translocation was determined in N+ cells. Data from 1500 cells/condition are shown. (**h**) Viral replication at 48hpi. (**i**) Representative western blot of Orf6, N, spike/S2 and β-Actin at 48hpi in infected cells +/-5µM ruxolitinib. Non-specific bands detected by polyclonal anti-spike primary antibody are indicated (see Extended Data Fig. 2a for Mock). (**j-m**) Quantification of Orf6 and N expression from five independent western blots of Calu-3 cells in the absence (**j**, Orf6; **k**, N) or presence of 5µM ruxolitinib (**l**, Orf6; **m**, N), normalized to spike over BA.2. (**n-q**) sgRNA expression of (**n**) Orf6, (**o**) N, (**p**) spike and (**q**) Orf3a normalized to Orf1a genomic RNA in Calu-3 cells at 48hpi, n=9. (**r**) Western blot of Calu-3 cells infected with Delta, BA.1, BA.2, BA.4 and BA.5 at 2000 E copies/cell showing Orf9b, Orf6, N and β-Actin expression at 48hpi+5µM ruxolitinib.
For b-f, h, j-q, one-way ANOVA with Dunnett's post-test was used to compare BA.2 with other variants. For g Kruskal-Wallis test was used to compare groups at 24hpi and 48hpi. Mean+/-SEM or individual datapoints are shown. hpi, hours post infection. sgRNA, subgenomic RNA. *, $p<0.05$; ***, $p<0.001$; n.s., not significant.

Figure 3

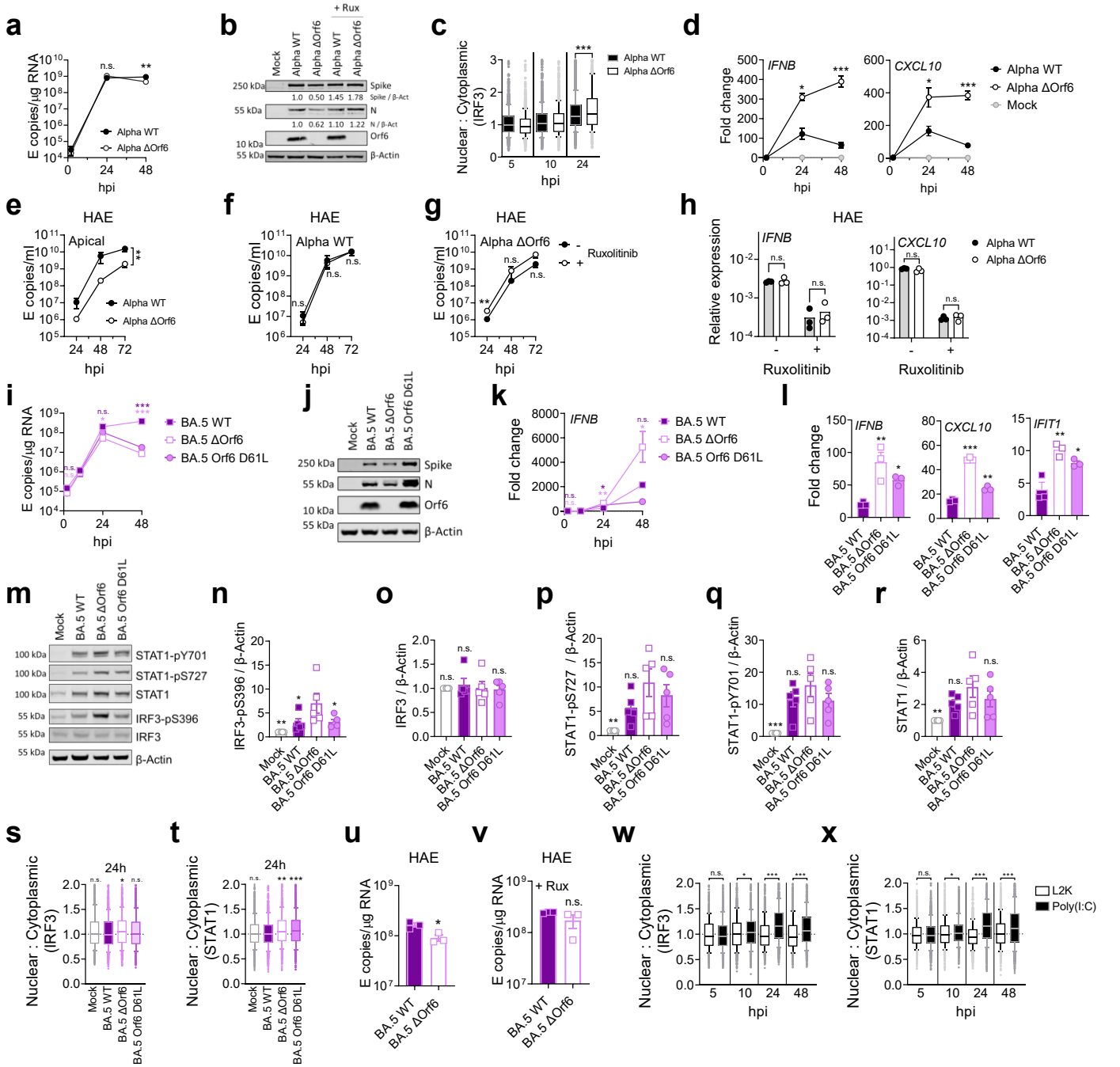

Fig. 3. Orf6 expression is a major determinant of enhanced innate immune antagonism by emerging VOCs.
(**a**) Replication of reverse genetic (RG) viruses parental Alpha WT and ΔOrf6 in Calu-3 cells infected with 2000 E copies/cell over time, n=3. (**b**) Western blot of RG virus infections in Calu-3 cells at 24hpi for spike, N, Orf6 and β-Actin +/-5µM ruxolitinib. (**c**) Quantification of IRF3 translocation detected by single-cell fluorescence microscopy over time. In infected cultures, translocation was determined in N+ cells. Data from 1500 cells/condition are shown. (**d**) *IFNB* and *CXCL10* expression in cells from (a) over time, n=3. (**e-i**) Primary bronchial human airway epithelial cells (HAEs) were infected with 1500 E copies/cell of the indicated variants in the presence or absence of 5µM ruxolitinib, n=3. Viral replication was measured by (**e**) viral release into apical washes over time. Replication measured by apical release in HAEs infected with (**f**) Alpha WT or (**g**) ΔOrf6 in the presence or absence of 5µM ruxolitinib. (**h**) *IFNB* and *CXCL10* expression in cells from (e). (**i**) Replication of RG viruses BA.5 WT, ΔOrf6 and Orf6 D61L isolates in Calu-3 cells infected with 2000 E copies/cell over time. (**j**) Western blot of RG virus infections in Calu-3 cells at 24hpi for spike, N, Orf6 and β-Actin. (**k**) *IFNB* expression in cells from (i) over time. (**l**) Expression of *IFNB*, *CXCL10* and *IFIT1* in Calu-3 cells at 24hpi with 2000 E copies/cell of the indicated viruses. (**m**) Western blot of STAT1-pY701, STAT1-pS727, total STAT1, IRF3-pS396, total IRF3, and β-Actin at 24hpi. Quantification of four independent western blots showing (**n**) IRF3-pS396, (**o**) total IRF3, (**p**) STAT1-pS727, (**q**) STAT1-pY701 and (**r**) total STAT1 over β-Actin at 24hpi. Quantification of (**s**) IRF3 and (**t**) STAT1 translocation detected by single-cell fluorescence microscopy over time. In infected cultures, translocation was determined in N+ cells. Data from 1500 cells/condition are shown. (**u, v**) Replication of BA.5 WT and ΔOrf6 in HAEs infected with 1500 E copies/cell in the (**u**) absence or (**v**) presence of 5µM ruxolitinib. Quantification of (**w**) IRF3 and (**x**) STAT1 translocation detected by single-cell fluorescence microscopy over time in Calu-3 cells stimulated with poly(I:C) or vehicle Lipofectamine2000 (L2K). Data from 1500 cells/condition are shown.
For indicated statistical comparisons at each time point in a, d-l, m, o-s, v and w one-way ANOVA with Dunnett's post-test was used. In c, x and y, groups were compared by Kruskal-Wallis test at each time point. For j and l, RG mutants were compared to WT using a two-way ANOVA and Bonferroni post-test. Colors indicate comparator (BA.5 ΔOrf6, purple; BA.5 Orf6 D61L, light pink). Mean+/-SEM or individual datapoints are shown. hpi, hours post infection. *, p<0.05 ; **, p<0.01; ***, p<0.001; n.s., not significant.

Figure 4

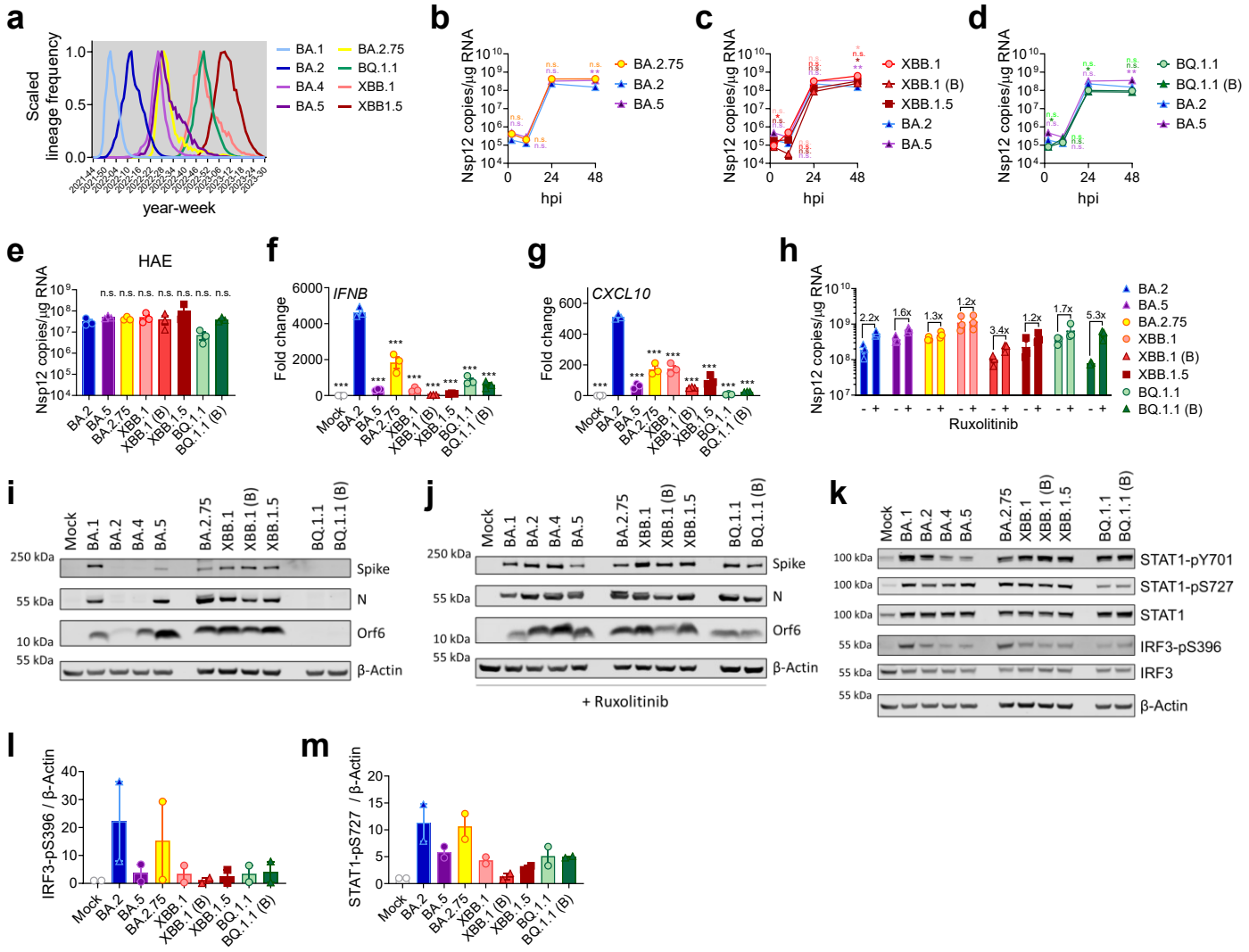

Fig. 4. Innate immune phenotype of dominant Omicron subvariants.
(**a**) Global SARS-CoV-2 variant sequence counts over time (scaled per variant), extracted from CoV-Spectrum using genomic data from GISAID. (**b-d**) Calu-3 cells were infected with 2000 Nsp12 copies/cell. Replication of Omicron subvariants compared to BA.2 (blue) and BA.5 (purple) measured by Nsp12 copies/µg RNA is shown for (**b**) BA.2.75 (yellow; O), (**c**) XBB-subvariants (XBB.1: light red, O; XBB.1 (B): red, Δ; XBB.1.5: dark red, □) and (**d**) BQ.1.1 (BQ.1.1: light green, O; BQ.1.1 (B): dark green, Δ) isolates. (**e**) HAEs were infected with 1500 Nsp12 copies/cell and intracellular Nsp12 copies measured at 72hpi. (**f**) *IFNB* and (**g**) *CXCL10* expression in Calu-3 cells infected with 2000 Nsp12 copies/cell of the indicated Omicron subvariants at 24hpi. (**h**) Viral replication of indicated variants in Calu-3 cells in the presence or absence of 5µM ruxolitinib at 48hpi. Numbers indicate fold change in replication in the presence of 5µM ruxolitinib. (**i,j**) Western blot of Orf6, N, spike and β-Actin at 48hpi in infected Calu-3 cells from (b-d) in the (**i**) absence or (**j**) presence of 5µM ruxolitinib. (**k**) Western blot of STAT1-pY701, STAT1-pS727, total STAT1, IRF3-pS396, total IRF3, and β-Actin in Calu-3 cells at 24hpi. Quantification of two independent western blots showing (**l**) IRF3-pS396 and (**m**) STAT1-pS727 over β-Actin at 24hpi.
For b-d, variant replication was compared to BA.2 at each time point using a two-way ANOVA and Bonferroni post-test. Colors indicate comparator (BA.5, purple; BA.2.75, yellow; XBB.1, light red; XBB.1 (B), red; XBB.1.5, dark red; BQ.1.1, light green; BQ.1.1 (B), dark green). For e-g, one-way ANOVA with Dunnett's post-test was used to compare all variants to BA.2.
Mean+/-SEM or individual datapoints are shown. hpi, hours post infection. *, $p<0.05$; **, $p<0.01$; ***, $p<0.001$; n.s., not significant.

Extended Data Figure 1

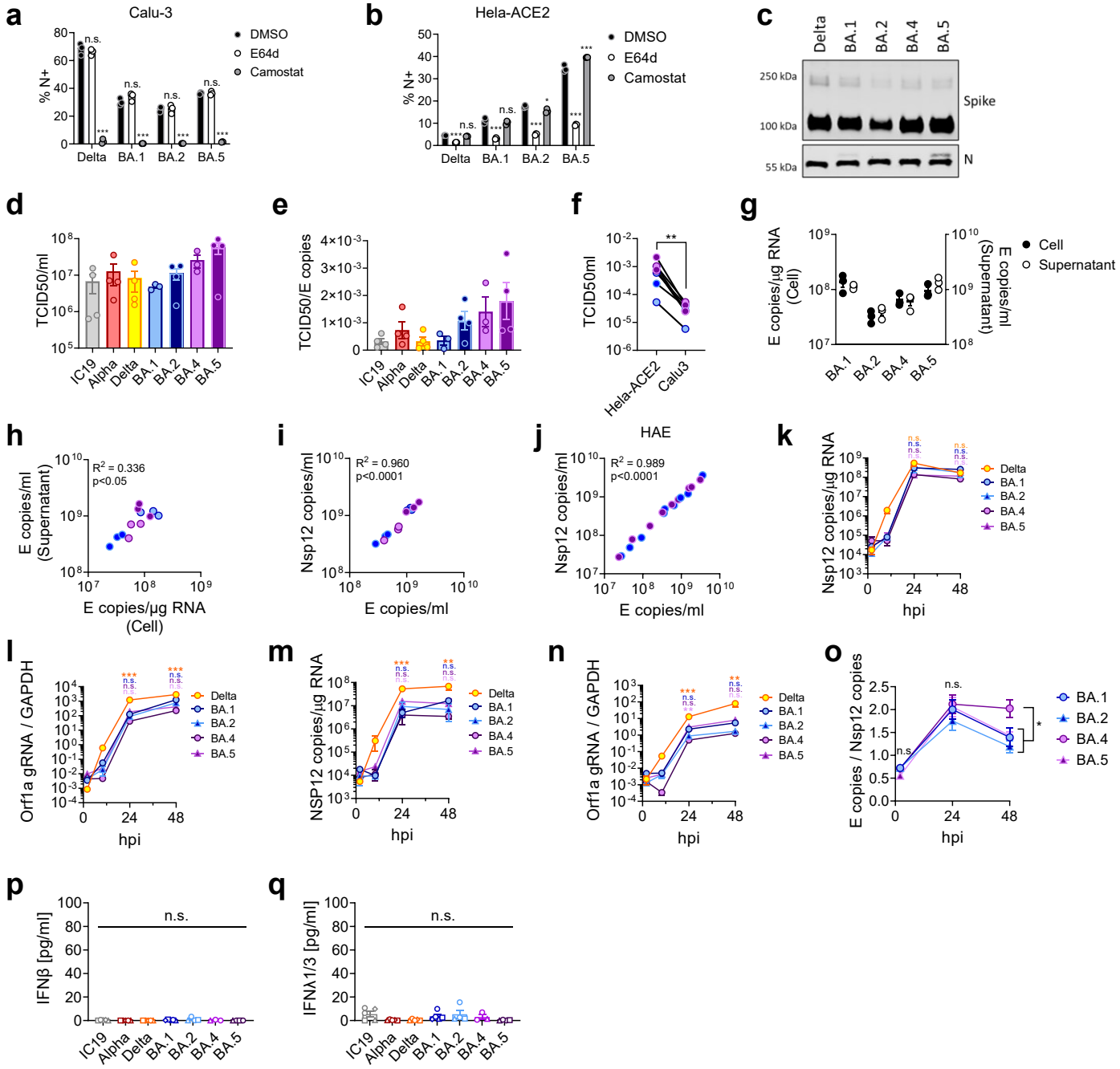

Extended Data Fig. 1. Replication measurements of SARS-CoV-2 variants.
(**a**) Calu-3 and (**b**) Hela-ACE2 cells were infected with 1000 E copies/cell of the indicated variants in the presence of DMSO (-), 25µM E64d or 25µM camostat. Infection levels were measured at 24hpi by nucleocapsid expression (% N+ by flow cytometry), n=3. (**c**) Representative western blot of spike and N in purified SARS-CoV-2 virions, n=2. (**d**) Quantification of viral stock used in Fig. 1 and 2 by TCID50/ml on Hea-ACE2 cells. (**e**) Ratio of TCID50/ml over E copies/ml for virus stocks from (d). (**f**) TCID50/ml of indicated virus stocks measured on ACE2-Hela or Calu-3 cells. (**g-i**) Calu-3 cells were infected with 2000 E copies/cell of the indicated variants. At 24hpi, cells and culture supernatant were harvested to determine intracellular viral replication and virus release. (**g**) Intracellular replication (Cell) and viral release (Supernatant) was determined by quantification of E copies at 24hpi. (**h**) Correlation graph of intracellular E copies and virus released into supernatant at 24hpi. (**i**) Correlation of Nsp12 and E gene copies in supernatants from (g). (**j**) Correlation of Nsp12 and E copies in apical washes from HAEs infected with BA.2 (blue) or BA.5 (purple) (samples from Fig. 4). Calu-3 cells were infected with 2000 E copies/cell and viral replication measured by (**k**) Nsp12 copies/µg RNA or (**l**) Orf1a gRNA/*GAPDH* in cells from Fig. 1a. Viral replication measured by (**m**) Nsp12 copies/µg RNA or (**n**) Orf1a gRNA/*GAPDH* in cells infected with 200 E copies/ml from Extended Data Fig. 2h. (**o**) E copies/Nsp12 copies ratio in Calu-3 cells over time calculated from three independent experiments. (**p**) IFNβ and (**q**) IFNλ1/3 levels detected in SARS-CoV-2 variant inoculum prepared from virus stocks prepped in Caco-2 cells.
For statistical comparison in a, b, k-q, one-way ANOVA with a Bonferroni post-test was used. For a, b, groups were compared to DMSO. For k-o, groups were compared to BA.2 and colors indicate comparator (Delta, yellow; BA.1, blue; BA.4, purple; BA.5, pink). For f, groups were compared by paired Student's t-Test. R^2 and p-values in h-j were calculated using simple linear regression. Mean+/-SEM or individual datapoints are shown. hpi, hours post infection. gRNA, genomic RNA. *, p<0.05 ; **, p<0.01; ***, p<0.001; n.s., not significant.

Extended Data Figure 2

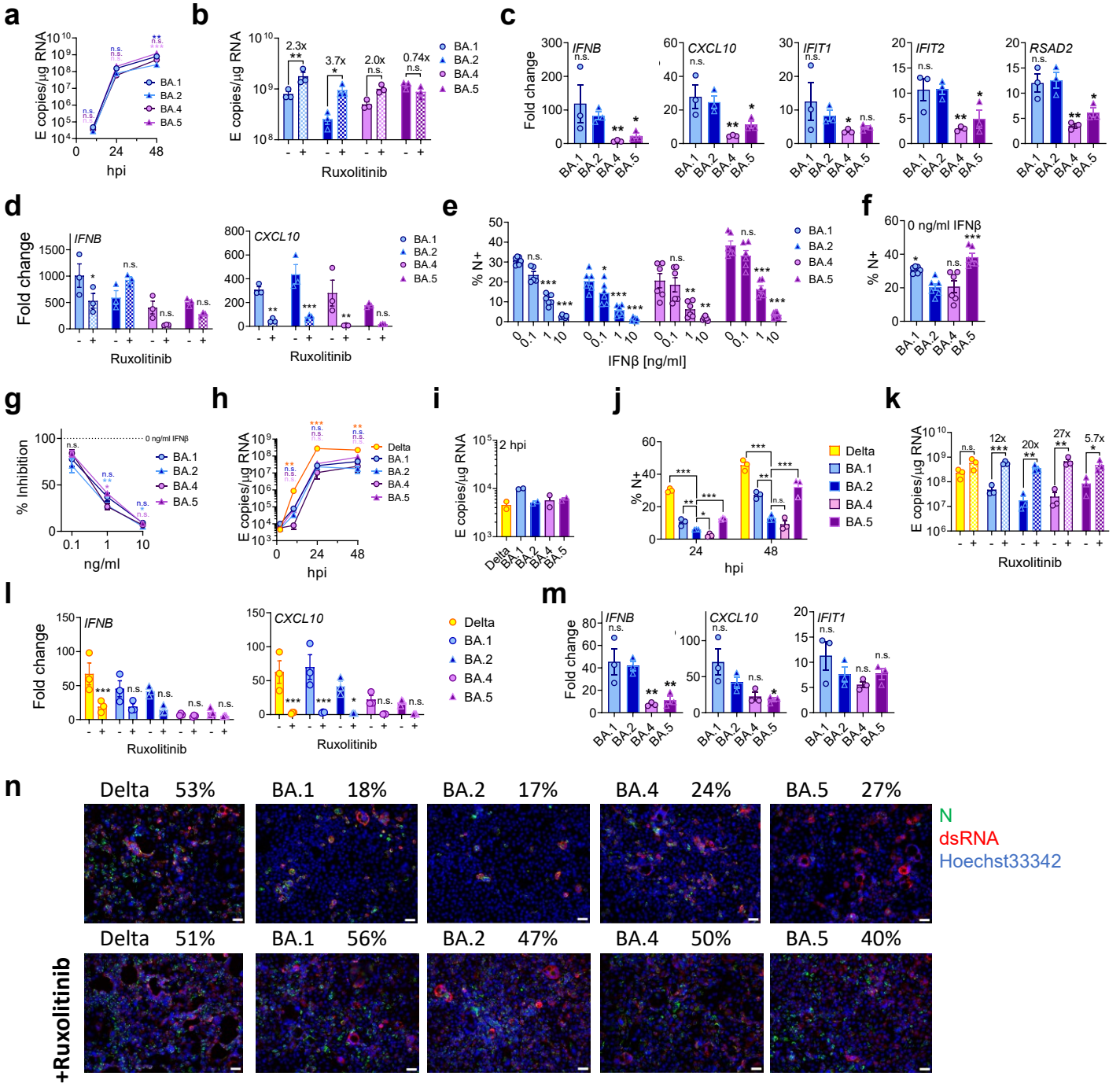

Extended Data Fig. 2. BA.5 displays enhanced innate immune antagonism during infection of airway epithelial cells. (**a-d**) Calu-3 infection with 2000 E copies/cell of BA.1 (blue; O), BA.2 (blue; Δ), BA.4 (purple; O) and BA.5 (purple; Δ), n=3. (**a**) Viral replication over time, n=3. (**b**) Viral replication of indicated variants in the presence or absence of 5µM ruxolitinib at 48hpi, n=3. (**c**) *IFNB*, *CXCL10*, *IFIT1, IFIT2* and *RSAD2* expression at 24hpi, n=3. (**d**) Expression of *IFNB* and *CXCL10* in the presence of ruxolitinib in cells from (c). (**e-g**) IFNβ-sensitivity of indicated variants during Calu-3 cell infection at 2000 E copies/cell. (**e**) Infection levels measured by % N+ at 24hpi at the indicated concentrations of IFNβ, n=6. (**f**) Infection levels in cells from (e) at 0ng/ml IFNβ, n=6. (**g**) Infection levels from (e) normalized to 0ng/ml IFNβ for each variant, n=6. (**h-m**) Calu-3 infection with 200 E copies/cell of Delta (yellow; O), BA.1 (blue; O), BA.2 (blue; Δ), BA.4 (purple; O) and BA.5 (purple; Δ), n=3. (**h**) Viral replication over time measured by RT-qPCR for intracellular E copies. (**i**) Viral E copies at 2hpi in cells from (h). (**j**) Infections levels measured by nucleocapsid expression (% N+ by flow cytometry). (**k**) Viral replication of indicated variants in Calu-3 cells from (a) in the presence or absence of 5µM ruxolitinib at 48hpi, n=3. (**l**) Expression of *IFNB* and *CXCL10* in the presence of ruxolitinib in cells from (h). (**m**) Expression of *IFNB, CXCL10* and *IFIT1* in infected cells at 24hpi in cells from (h). (**n**) Fluorescence microscopy of Calu-3 cells infected at 2000 E copies/cell at 48hpi in the presence or absence of 5µM ruxolitinib. Percentage infection quantified by dsRNA-positive cells is indicated per condition. Nucleocapsid, green; dsRNA, red; Hoechst33342, blue. Representative images shown. Scale bar, 50µm.

For statistical comparisons, one-way ANOVA and Dunnett's post-test were used. Groups were compared as indicated or with BA.2. For e, comparisons were made against 0ng/ml IFNβ for each variant. Colors in a, g and h indicate comparator (Delta, yellow; BA.1, blue; BA.4, purple; BA.5, pink). Mean+/-SEM or individual datapoints are shown. hpi, hours post infection. *, p<0.05 ; **, p<0.01; ***, p<0.001; n.s., not significant.

Extended Data Figure 3

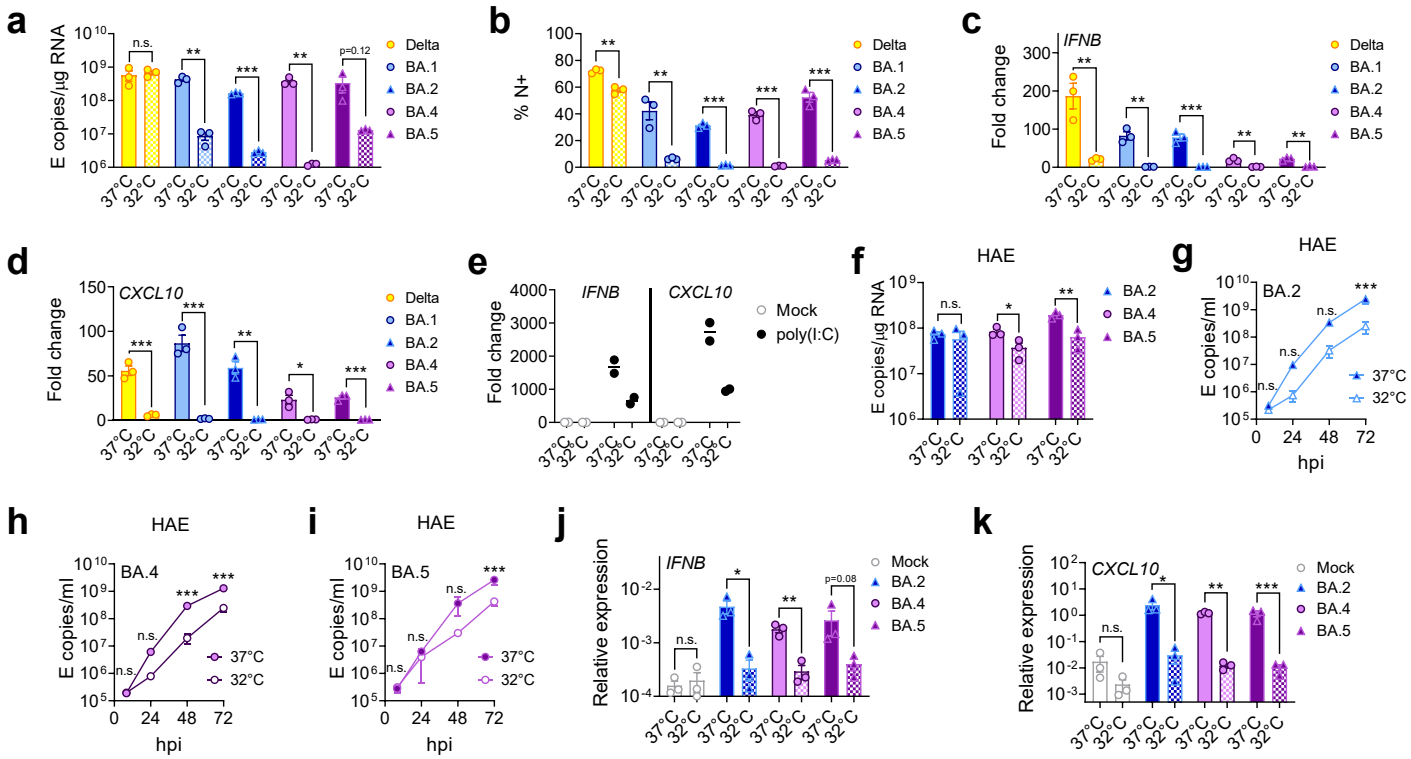

Extended Data Fig. 3. Entry and replication characteristics of Omicron subvariant BA.5.
(**a-d**) Calu-3 cells were infected with 2000 E copies/cell at 37ºC or 32ºC, n=3. (**a**) Viral replication by RT-qPCR and (**b**) infection levels by flow cytometry at 24hpi. (**c**) *IFNB* and (**d**) *CXCL10* expression in cells from (a). (**e**) *IFNB* and *CXCL10* expression in response to poly(I:C) transfection in Calu-3 cells at 24h of stimulation, n=2. (**f-k**) Primary bronchial human airway epithelial cells (HAEs) were infected with 1500 E copies/cell of the indicated variants at 37ºC or 32ºC, n=3. Viral replication was measured by (**f**) intracellular E copies at 72hpi and viral release of (**g**) BA.2, (**h**) BA.4 and (**i**) BA.5 into apical washes over time. Relative expression of (**j**) *IFNB* and (**k**) *CXCL10* normalized to *GAPDH* in cells from (f). Fold changes are normalized to mock.
Pairwise comparisons were performed using an unpaired two-tailed Student's t-Test as indicated. For g-i, two-way ANOVA with a Bonferroni post test was used to compare temperatures at each time point. Mean+/-SEM or individual datapoints are shown. hpi, hours post infection. *, p<0.05 ; **, p<0.01; ***, p<0.001; n.s., not significant or exact p-value given (k).

Extended Data Figure 4

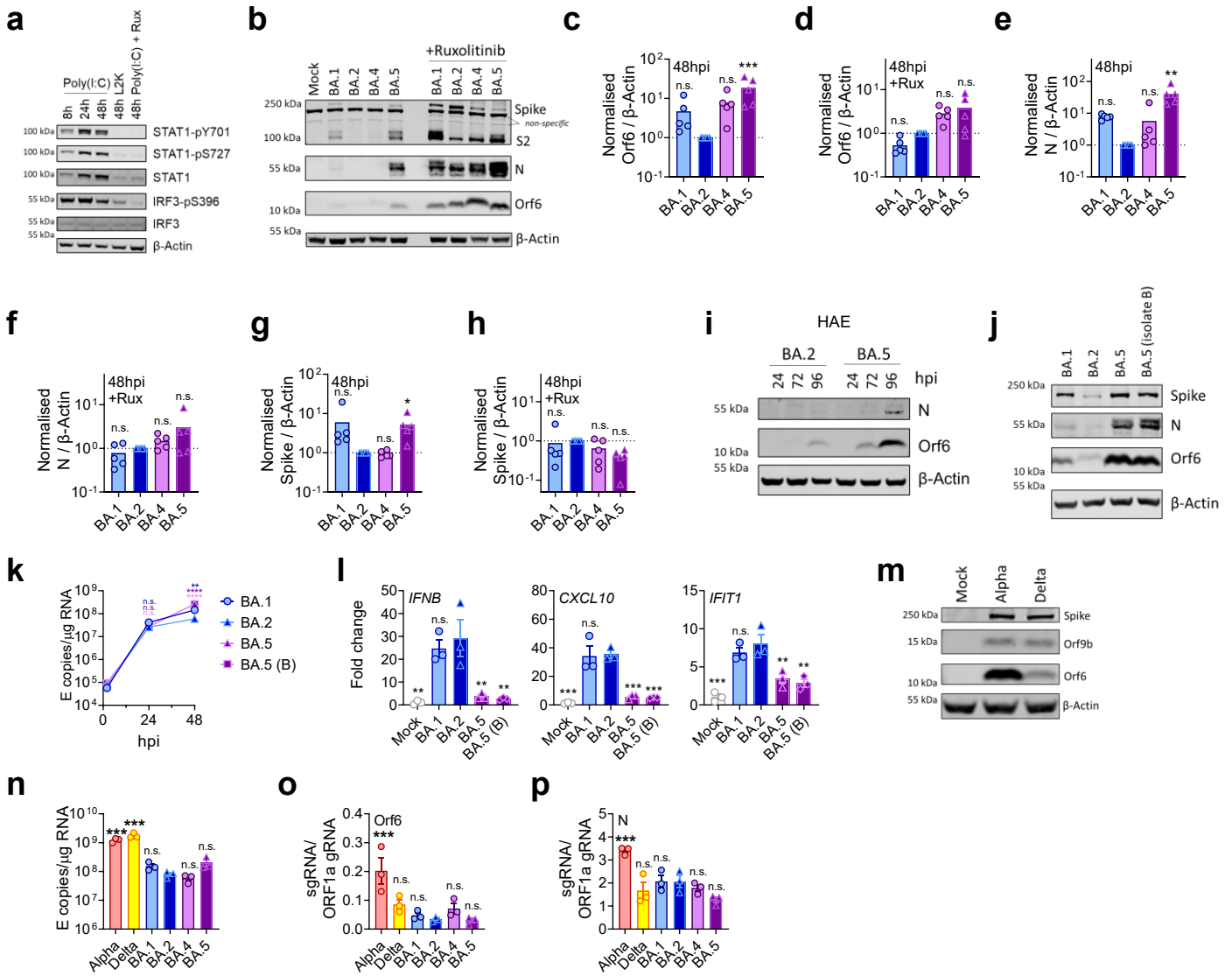

Extended Data Fig. 4. BA.5 efficiently expresses SARS-CoV-2 innate antagonists during airway epithelial cell infection. (**a**) Western blot of Calu-3 cells treated with poly(I:C), vehicle control lipofectamin2000 (L2K) or 5µM ruxolitinib where indicated. STAT1-pY701, STAT1-pS727, total STAT1, IRF3-pS396, total IRF3, and β-Actin are shown at indicated time points. (**b**) Western blot of Orf6, N, spike/S2 and β-Actin at 48hpi in infected Calu-3 cells +/-5µM ruxolitinib. Non-specific bands detected by polyclonal anti-spike primary antibody are indicated. (**c-h**) Quantification of viral protein expression from five independent western blots of infected Calu-3 cells at 48hpi +/-5µM ruxolitinib. (**c,d**) Orf6, (**e,f**) N and (**g**,**h**) spike were normalized to β-Actin over BA.2. (**i**) Western blot of Orf6 and N expression by HAEs infected with 1500 E copies/cell of BA.2 or BA.5 over time. (**j**) Western blot of Orf6, N, spike and β-Actin at 48hpi in Calu-3 cells infected with BA.1, BA.2 and two independent BA.5 isolates. (**k,l**) Calu-3 cells were infected with BA.1, BA.2 and two independent BA.5 isolates and (**k**) replication measured over time. (**l**) Expression of *IFNB*, *CXCL10* and *IFIT1* is shown at 24hpi in cells from (k). (**m**) Western blot of Orf9b, Orf6, spike and β-Actin at 24hpi in Calu-3 cells infected with the indicated variants at 2000 E copies/cell. (**n**) Viral replication in Calu-3 cells by RT-qPCR at 24hpi, n=3. (**o**) Orf6 and (**p**) N sgRNA expression in cells from (n), n=3.

For c-h, l, n-o, one-way ANOVA with Dunnett's post-test was used to compare BA.2 with other variants. For k, two-way ANOVA with a Bonferroni post-test was used to compare variants with BA.2 at each time point. Colors indicate comparator (BA.1, blue BA.5, purple; BA.5 (B), pink). Mean+/-SEM or individual datapoints are shown. hpi, hours post infection. sgRNA, subgenomic RNA. *, $p<0.05$; ***, $p<0.001$; n.s., not significant.

Extended Data Figure 5

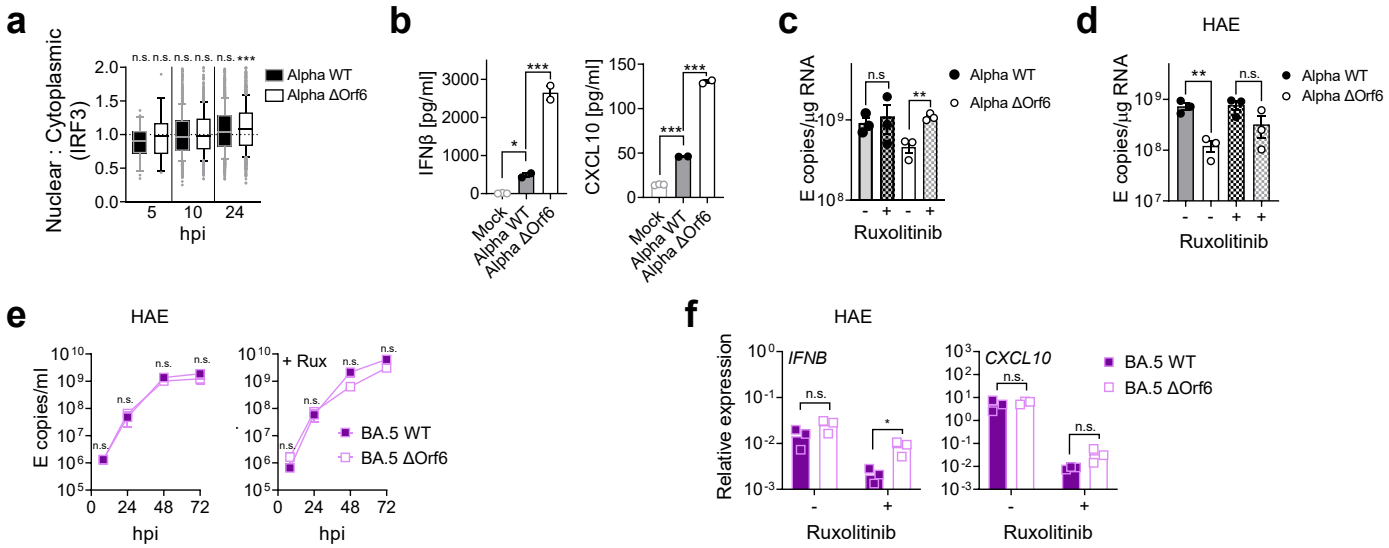

Extended Data Fig. 5. Orf6 expression is a major determinant of enhanced innate immune antagonism by emerging VOCs. (**a**) Quantification of IRF3 translocation in Calu-3 cells infected with Alpha WT and ΔOrf6 detected by single-cell fluorescence microscopy over time. Data from 1500 cells/condition are shown. (**b**) IFNβ and CXCL10 secretion from infected Calu-3 cells measured at 48hpi, n=2. (**c**) Viral replication in the presence or absence of 5µM ruxolitinib at 48hpi in cells from (Fig. 3a). (**d**) Primary bronchial human airway epithelial cells (HAEs) were infected with 1500 E copies/cell of the indicated variants in the presence or absence of 5µM ruxolitinib, Intracellular E copies are shown (n=3). Apical washes are shown in Fig. 3e-g. (**e, f**) Infection of HAEs with BA.5 WT or BA.5 ΔOrf6 with 1500 E copies/cell showing (**e**) viral release into apical washes over time or (**f**) *IFNB* and *CXCL10* expression at 72hpi.

For a, Kruskal-Wallis test was used to compare groups to mock at each time point. In b-d, one-way ANOVA with Dunnett's post-test was used to compare groups as indicated. For e, groups were compared at each time point using a two-way ANOVA with a Bonferroni post-test. Groups in f were compared by paired Student's t-Test. *, $p<0.05$; **, $p<0.01$; ***, $p<0.001$; n.s., not significant.

Extended Data Figure 6

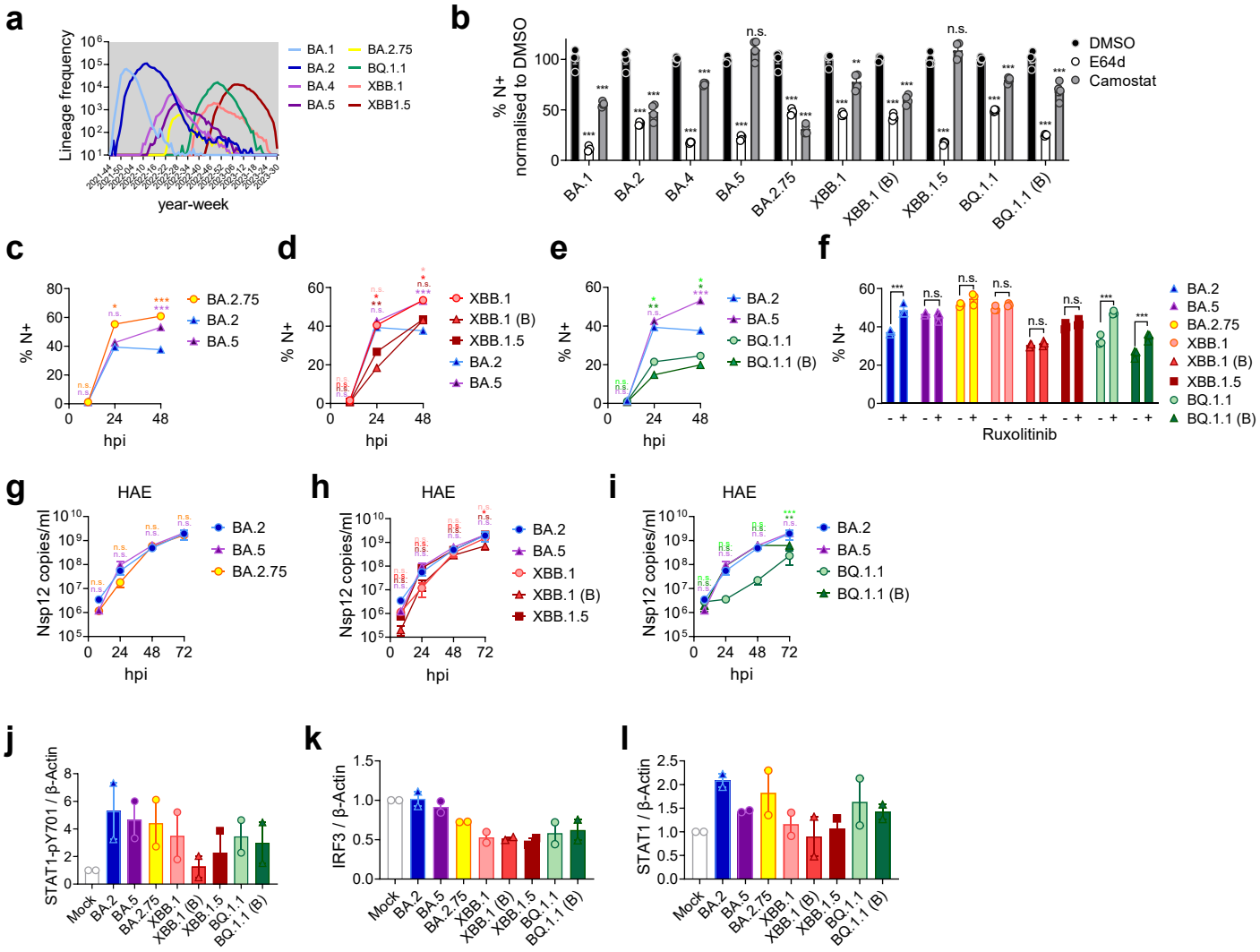

Extended Data Fig. 6. Innate immune phenotype of dominant Omicron subvariants.
(**a**) Absolute global SARS-CoV-2 variant sequence counts over time, extracted from CoV-Spectrum using genomic data from GISAID. (**b**) ACE2/TMPRSS2-A549 cells were infected with 2000 Nsp12 copies/cell of the indicated SARS-CoV-2 variants in the presence of DMSO, 25µM E45d or 25µM camostat. Infection levels were determined by N-positivity at 24hpi. (**c-e**) SARS-CoV-2 Omicron subvariants infection of Calu-3 cells determined by N-positivity over time for the indicated subvariants in cells from Fig. 4b-d with (**c**) BA.2.75 (yellow; O), (**d**) XBB-subvariants (XBB.1: light red, O; XBB.1 (B): red, Δ; XBB.1.5: dark red, □) and (**e**) BQ.1.1 (BQ.1.1: light green, O; BQ.1.1 (B): dark green, Δ) isolates shown. (**f**) Infection levels of indicated variants in Calu-3 cells in the presence or absence of 5µM ruxolitinib at 48hpi in cells from Fig. 4h. (**g-i**) Primary bronchial human airway epithelial cells (HAEs) were infected with 1500 E copies/cell of the indicated variants. Viral replication was measured by viral release into apical washes over time in cells from Fig. 4e. (**g**) BA.2.75, (**h**) XBB-subvariants and (**i**) BQ.1.1 isolates are shown compared to BA.2 (blue) and BA.5 (purple). Quantification of two independent western blots showing (**j**) STAT1-pY701, (**k**) total IRF3 and (**l**) total STAT1 over β-Actin at 24hpi.
For b, treatments were compared to DMSO for each variant using one-way ANOVA and Dunnett's post-test. For c-i, variant infection levels were compared to BA.2 at each time point by two-way ANOVA and Bonferroni post-test. Colors indicate comparator (BA.5, purple; BA.2.75, yellow; XBB.1, light red; XBB.1 (B), red; XBB.1.5, dark red; BQ.1.1, light green; BQ.1.1 (B), dark green). Mean+/-SEM or individual datapoints are shown. hpi, hours post infection. *, $p<0.05$; **, $p<0.01$; ***, $p<0.001$; n.s., not significant.

Extended Data Table 1. Orf6 mutations detected in the Omicron subvariants

	BA.1	BA.2	BA.4	BA.5
A27259C (synonymous)	+	+	+	–
G27382C, A27383T, T27384C (non-synonymous: D61L)	–	+	+	–

Presence of Orf6 mutations in BA.1, BA.2, BA.4 and BA.5 at the indicated positions compared to the reference sequence hCoV-19/Wuhan/WIV04/2019 (WIV04) (EPI_ISL_402124). Nucleotide and (non-synonymous amino acid) changes indicated. No mutations were detected in the region of the M gene surrounding the Orf6 TRS at position 27041-27046 (core TRS ACGAAC).

Extended Data Table 2. Nucleocapsid (N) mutations detected in the Omicron subvariants

	BA.1	BA.2	BA.4	BA.5
C28311T (non-synonymous: P13L)	+	+	+	+
A28330G (synonymous)	–	–	–	+
A28363T (synonymous)	+	+	+	+
Deletion 28364-28372 (31-33del)	+	+	+	+
C28724T (non-synonymous: P151S)	–	–	+	–
G28881A, G28882A (non-synonymous R203K[†])	+	+	+	+
G28883C (non-synonymous G204R[†])	+	+	+	+
A29510C (non-synonymous S413R)	–	+	+	+

Presence of N mutations in BA.1, BA.2, BA.4 and BA.5 at the indicated positions compared to the reference sequence hCoV-19/Wuhan/WIV04/2019 (WIV04) (EPI_ISL_402124). Nucleotide and (non-synonymous amino acid) changes indicated. BA. 1, BA.2, BA.4 and BA.5 carry nucleotide substitution A28271T, changing their Kozak initiation context from adequate (A in −3, T in +4) to the weak (T in −3, T in +4) as previously described[16].
[†] The non-synonymous mutations R203K-G204R confer a partial TRS for N* sgRNA[16].